COLLEGE DOCTORAL PAYS DE LA LOIRE
ED MATIERE, MOLECULES, MATERIAUX & GEOSCIENCES

Nantes Université

THESE DE DOCTORAT DE

NANTES UNIVERSITE
ECOLE DOCTORALE N° 596
Matière, Molécules, Matériaux et Géosciences
Spécialité : « Sciences des Matériaux »

Par
Hannah NICKLES JÄKEL

Evaluating and mitigating beam damage in battery materials: Advancing *in situ* STEM-EELS through alternative scanning approaches

Évaluation et réduction des dommages induits par un faisceau électronique dans les matériaux de batteries: vers une amélioration de la caractérisation STEM-EELS *in situ* grâce à des approches de balayage alternatives

Thèse présentée et soutenue à Nantes, le 04/12/2026

Rapporteurs avant soutenance :

Carine Davoisne	Maître de conférences, Université Picardie Jules Verne
Johan Verbeeck	Professeur, Université d'Anvers, Belgique

Composition du Jury :

Président :	Prénom Nom	Fonction et établissement d'exercice (8)*(à préciser après la soutenance)*
Examinateurs :	Pascale Bayle Guillemaud	Directrice de recherche, IRIG, CEA Grenoble
	Santhana Eswara	Directeur de recherche, LIST Luxembourg
	Carine Davoisne	Maître de conférences, Université Picardie Jules Verne
	Johan Verbeeck	Professeur, Université d'Anvers, Belgique
Dir. de thèse :	Philippe Moreau	Professeur, Nantes Université
Co-dir. de thèse :	Patricia Abellan	Chargée de recherche, CNRS, Nantes

Invité(s)

Maurice Peemen	Senior scientist, Thermo Fisher Scientific

Theory and Background studies

1 Characterization Methods: Electron Microscopy

This chapter provides a brief overview of the most relevant characterization methods used in this thesis. First, Scanning Transmission Electron Microscopy (STEM) is introduced, including the two spectroscopy-methods Energy Dispersive X-Ray Spectroscopy (EDS) and Electron Energy Loss Spectroscopy (EELS) which provide information on elemental composition and chemistry. Lastly an overview of Liquid-Phase TEM (LP-TEM) will be given, which enables to study damage dynamics in liquids.

1.1 Scanning Transmission Electron Microscopy (STEM)

In Figure 1 a schematic overview for a typical Transmission Electron Microscope (TEM) set-up with the option for Scanning Transmission Electron Microscopy (STEM) is shown. In STEM a convergent electron beam is scanned across a sample and the image is formed from signal detected at each irradiated pixel.

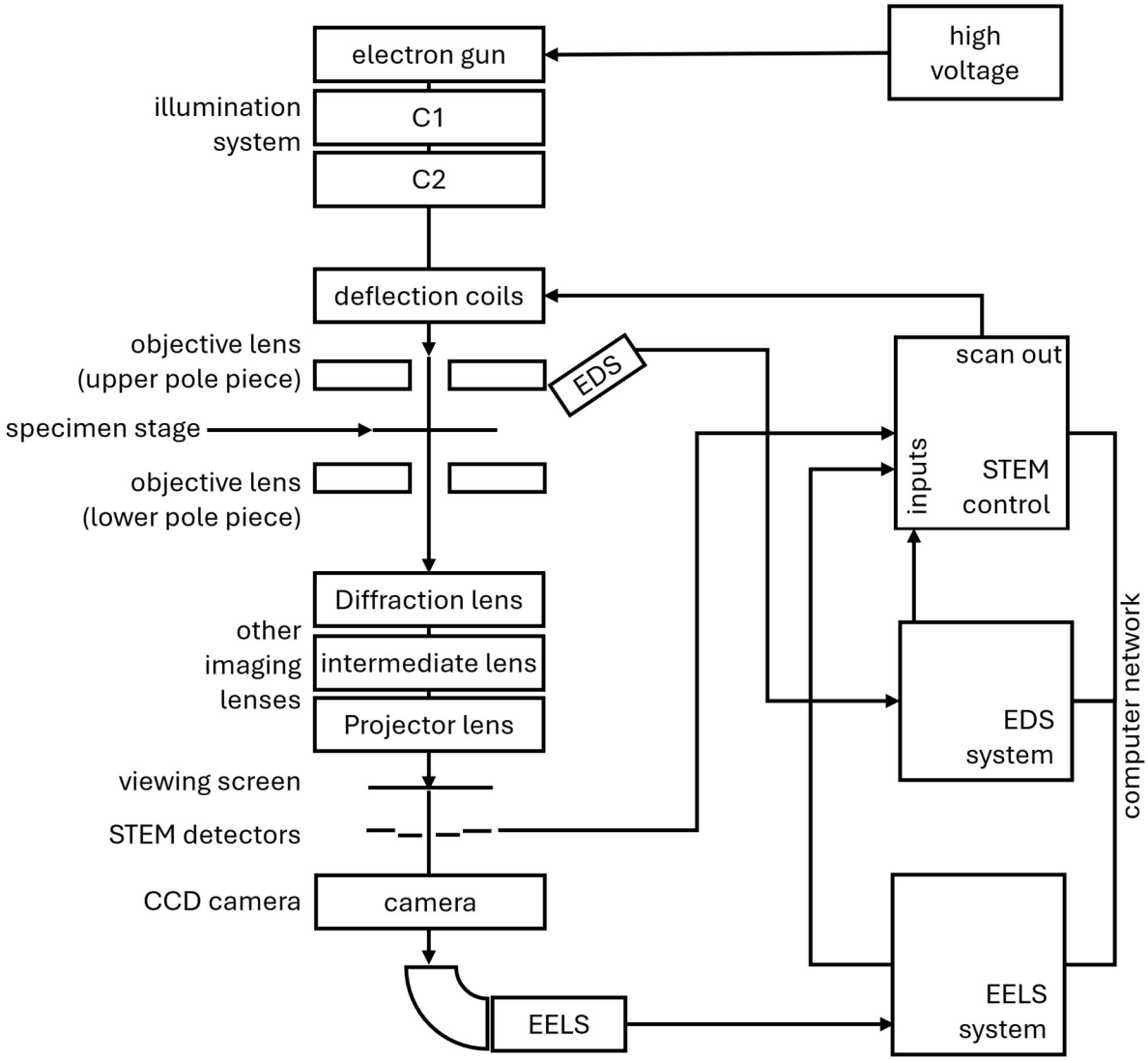

Figure 1. Schematic overview of a typical TEM set up with option for STEM (after [1])

Electrons are generated from an electron gun, which are typically either a thermionic source, a cold field emitter gun (FEG) or a Schottky FEG. A monochromator can be used to increase energy resolution.

Electrons are focused into a converged electron probe with magnetic lenses and apertures and the probe is scanned across the sample with a deflection coil system. The scan engine will be further discussed later in Chapter 4. Depending on the electron beam matter interactions, different signals can be detected with various detection systems.

In Figure 2, a schematic overview of electron beam sample interactions is given. Incident electrons interact with the sample via Coulomb interactions. Interactions of the incident electrons with the atomic nuclei results in high angle elastic scattering with no to little energy loss, which can induce phonons (collective atomic vibration). Coulomb interactions of fast incident electrons with atomic electrons result in an energy transfer to the sample and inelastic scattering with lower angles [2]. Inelastic interactions can result in core excitations, where an incident electron interacts with a core electron and subsequent relaxation of other core or valence electrons filling the empty core electron site, can lead to emittance of x-rays or Auger electrons [2]. Other inelastic interactions include interband transitions, where for insulators and semiconductors valence electrons are excited above the energy gap, which can result in secondary electron (SE) emission and or permanent radiolysis damage. Alternatively, relaxation of the excited state can result in photon emission (cathodoluminescence, CL) or heat. In another inelastic interaction plasmons, a collective oscillation of valence electrons, can be induced, which can decay by heat, interband transitions or SE creation. While elastic and inelastic interactions are used for different imaging and spectroscopy insights, these interactions can also lead to damage, which will be further discussed in Chapter 2 Electron beam matter interactions and mitigation techniques.

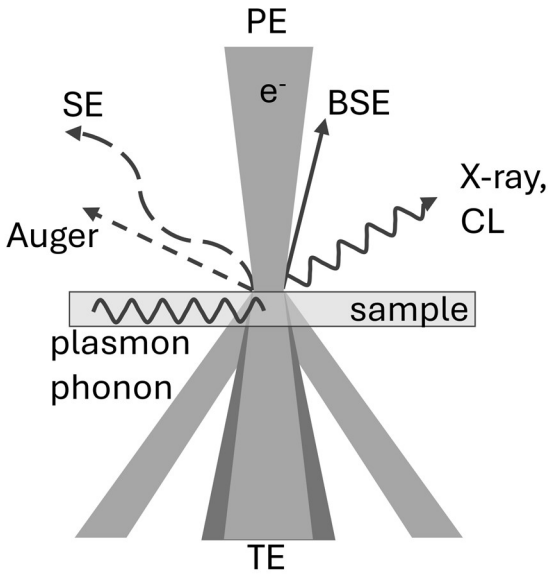

Figure 2. Schematic overview of electron-beam sample interactions with PE: primary electrons, TE: transmitted electrons, BSE: back-scattered electrons, SE: secondary electrons. (after [3,4]).

Most common imaging detectors include bright field (BF), ADF (annular dark field) and HAADF (high angle annular dark field) detectors. BF detectors collect on-axis to small angle scattered electrons (<10mrad), while ADF detectors detects signal scattered in low to medium angles (10-50mrad). The HAADF detector detects electrons scattered in high angles (>50mrad) and as high angle scattering is mostly proportional to the atomic number of the scattering atoms it provides Z-contrast imaging. [1,2,5].

Beside imaging, spectroscopy is possible, like EDS and EELS, which rely on inelastic electron matter interactions.

1.2 Energy Dispersive X-ray Spectroscopy (EDS)

EDS can give insights on the elemental distribution in the sample. EDS detectors, which are placed in the column above the sample (see Figure 1), collect x-rays emitted from inelastic interactions between electron-beam and sample (as described above). Emitted x-rays can be detected with silicon drift detectors. EDS can give quantitative and qualitative analysis of elemental sample composition, while it is not sensitive to differences in chemical bonding. For investigating battery materials, EDS holds the inherent disadvantage that Lithium cannot be detected in most common EDS detectors.

1.3 Electron Energy Loss Spectroscopy (EELS)

Electron Energy Loss Spectroscopy (EELS) detects how much energy the transmitted beam lost by electron-matter interactions. Depending on the inelastic interactions, EELS can give information on elemental distribution, bonding states and chemistry in the sample and sample thickness.

Electrons transmitted through the sample enter the EELS spectrometer, where a magnetic prism, focuses, deflects and disperses the electrons by their energy. The resulting electron energy distribution is recorded with a CCD or direct electron camera. In STEM-EELS, at each pixel a spectrum can be detected resulting in a spectrum image (SI), which gives spatially resolved spectral information

In Figure 3 an exemplary EEL spectrum is displayed. EEL spectra can be divided in low loss (<50eV) and high loss (>50eV) [2]. The zero-loss peak (ZLP) has the highest intensity and is composed from electrons with no to very low energy loss. Next to the ZLP interband transition peaks can be observed, which can give insights on optical properties, chemistry changes and defect evolution. Also, bandgap, exciton peaks and surface and bulk plasmons can be observed in the low loss region. The plasmon peak is sensitive to changes in valence electron density, heat, composition of alloys and thickness. In the high loss, core excitations can be found that relate to the energy needed to ionize a core electron and are therefore element specific. Examples are given in Figure 3 for the Li K-edge for LiF and in Figure 4 for the carbon K-edge of diethyl carbonate.

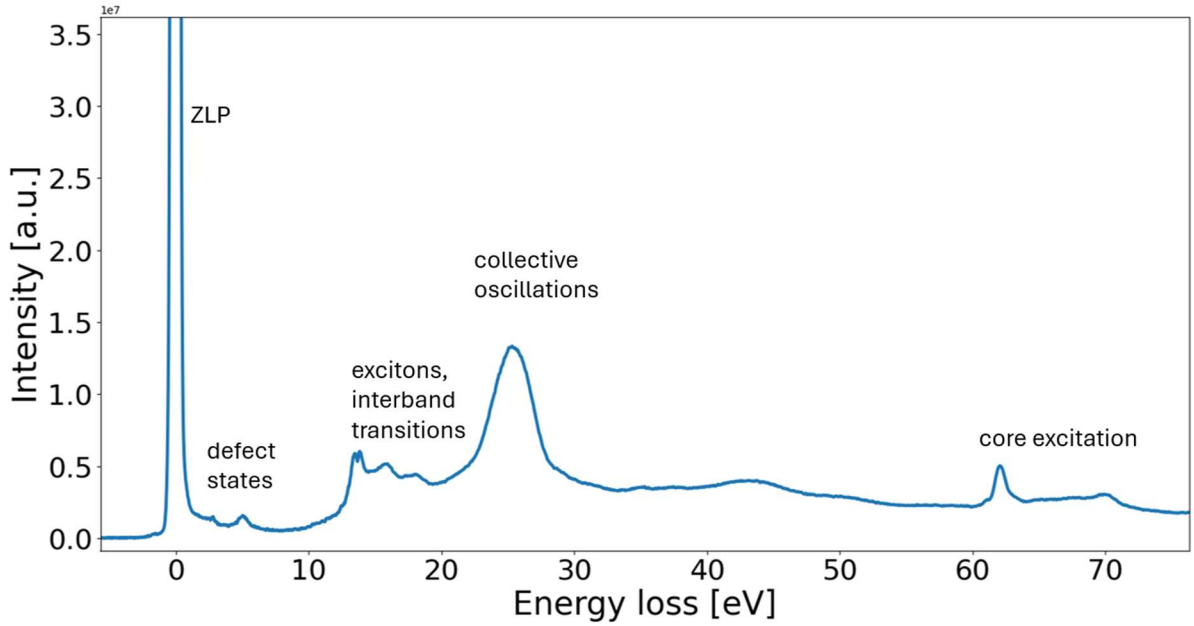

Figure 3. Exemplary EEL spectrum of LiF with ZLP, interband transitions, plasmon peak and core excitation for Li K-edge.

After background correction, the edge area can be used for quantitative analysis. The fine structure of the ionization edge can give insights on the energy band structure of the material. In the C K-edge example the different peaks correlate to different transitions from the C 1s to σ* or π* antibonding levels in diethyl carbonate. After losing energy due to ionization the same electron might lose

additional energy by inducing a plasmon before exiting the sample. This results in additional signal above the ionization edge. The plasmon contribution to the edge-signal can be removed by deconvolution, as can be seen in Figure 4, where Fourier ratio deconvolution with the low loss spectrum reduces intensity in the tail of the C edge.

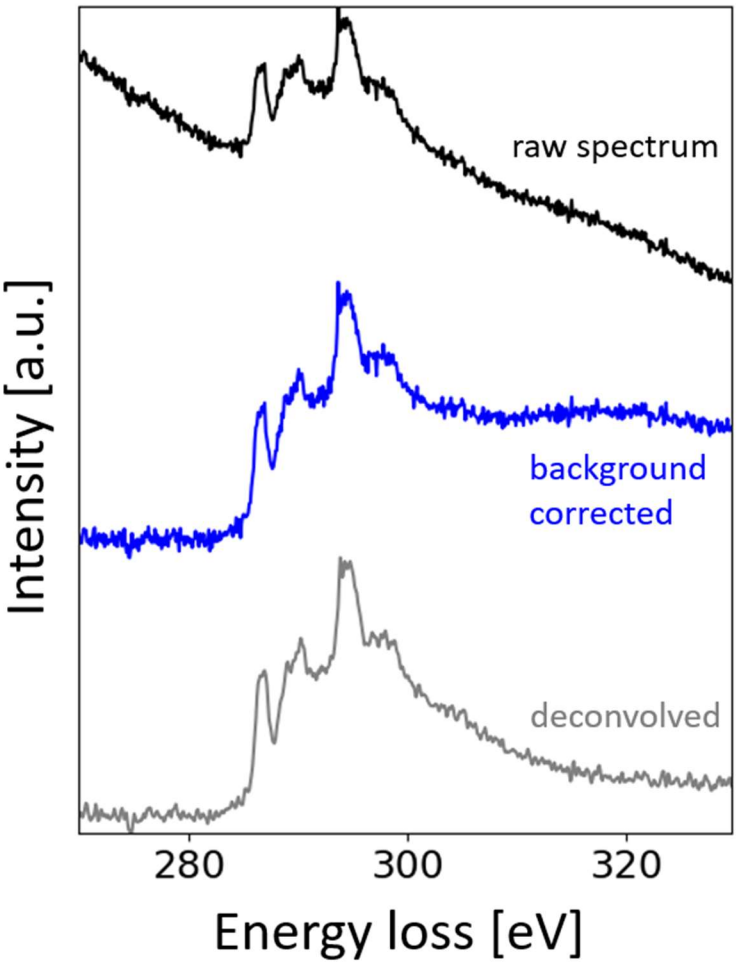

Figure 4. C K-edge for diethyl carbonate (DEC), with top to bottom: raw spectrum, background subtracted spectrum and spectrum Fourier ratio deconvolved with its low-loss region.

From EELS spectra the relative thickness can be calculated with the log ratio method:

$$\frac{t}{\lambda} = ln(I_t/I_0)$$

with the thickness t, mean free path for inelastic scattering λ, integrated intensity of the ZLP I_0 and integrated intensity of total EEL spectrum I_t [2].

1.4 Liquid Phase Transmission Electron Microscopy

Liquid-Phase TEM (LP-TEM) enables to study liquids in a TEM. LP-TEM has a wide variety of applications, ranging from life science studies with water as a more native environment to atomically resolved nucleation, growth and etching of particles. To protect the sensitive high vacuum set-up in a TEM, a thin liquid layer is encapsulated between electron transparent membranes in a liquid cell set-up. Most commonly these membranes are either graphene or silicon nitride. Liquid cells with integrated electrodes enable the investigation of electrochemical processes. SEI growth and dendrite formation were imaged [6–8]. In combination with STEM-EELS electrochemistry liquid cells enable high resolution chemistry mapping insights into interfacial battery processes and the potential to unravel

battery failure mechanisms that are holding back innovative battery designs. In practice however EELS is hindered by the liquid cell design, where liquid layers are bulging due to the high vacuum environment inside the TEM, leading to inhomogeneous liquid layers. The difference between liquid thickness at the center of the liquid cell compared to the border can be larger by more than a factor of two [9]. Lodico et al. [10] used a vacuum loading procedure to overcome this problem and were able to investigate the operando SEI formation with STEM-EELS. Nevertheless, their STEM-EELS insights on battery interface dynamics were limited to about 10nm resolution, which is larger than the SEI layer thicknesses reported. Also, time resolution was limited to a single frame, where the slow scan direction of the frame was used to compare differences in time. Spatial and temporal resolution is hindered by the electron beam alterations induced during the scan.

For a lithium battery set-up in an electrochemical liquid cell, there are many electronically insulating components, a part of electrodes, e.g. organic solvent, the salt in the electrolyte and the silicon nitride TEM membranes. Electronically insulating materials are easily affected by radiolysis and charging processes, which can lead to solvated electrons, radicals, bubble formation and charge induced diffusion, introducing alternative reaction pathways and disturbing investigation of pristine electrochemical dynamic processes.

Electron beam interactions with organic solvents as well as the influence of the silicon nitride membrane are not well understood yet. Further understanding of damage mechanisms in relevant organic solvents for being able to differentiate between electron beam induced and electrochemistry effects. Also, innovative damage mitigation techniques are necessary, to increase achievable spatial and temporal resolution in STEM-EELS experiments of interfacial battery processes.

In this work we will focus on diethyl carbonate DEC, an organic solvent commonly used in electrolytes. Theory on radiolysis damage in liquids and DEC will be discussed in Chapter 2.8. Electron beam induced damage in DEC and alternative scan patterns as a potential damage mitigation technique will be investigated experimentally in Chapter 6. The liquid cell set-up used in this work will be introduced in Chapter 3.2.

1.5 TEMs used in this thesis

In Figure 5 the two different TEMs are displayed that were used in this work. Most of the experiments were acquired with the Nan'Themis (see Figure 5a), the STEM at the Institut des Matériaux de Nantes Jean Rouxel (IMN) in Nantes, except the alternative scan EELS experiments on LiF FIB lamellas (see Chapter 5.2), which were acquired on an Iliad microscope in Eindhoven (see Figure 5b), thanks to a collaboration with Thermo Fisher Scientific in the OPINCHARGE european project.

The Nan'Themis is a Cs-probe corrected and monochromated Themis Z G3 (Thermo Fisher Scientific) STEM with a X-FEG Schottky gun and alignments for acceleration voltages of 80, 200 and 300kV. With the monochromator an energy resolution of about <0.1eV is possible to achieve, while in practice usually an energy resolution of approximately 0.3eV is used. It is equipped with a 4-detector SuperX system EDS detector for EDS spectroscopy and for EEL spectroscopy with a GIF Quantum ERS 966 spectrometer (Gatan), a K2 Summit direct electron detection camera (Gatan) and a US1000 CCD camera.

The Iliad is equipped with an Iliad EELS Spectrometer and Energy Filter with a Zebra EELS detector, consisting of 5 strips and allowing therefore multi-EELS acquisitions. The TEM was operated with a monochromator at 300kV. With the monochromator an energy resolution of about <0.03eV (at 60kV) is possible to achieve, while in practice usually an energy resolution of approximately 0.14eV were used.

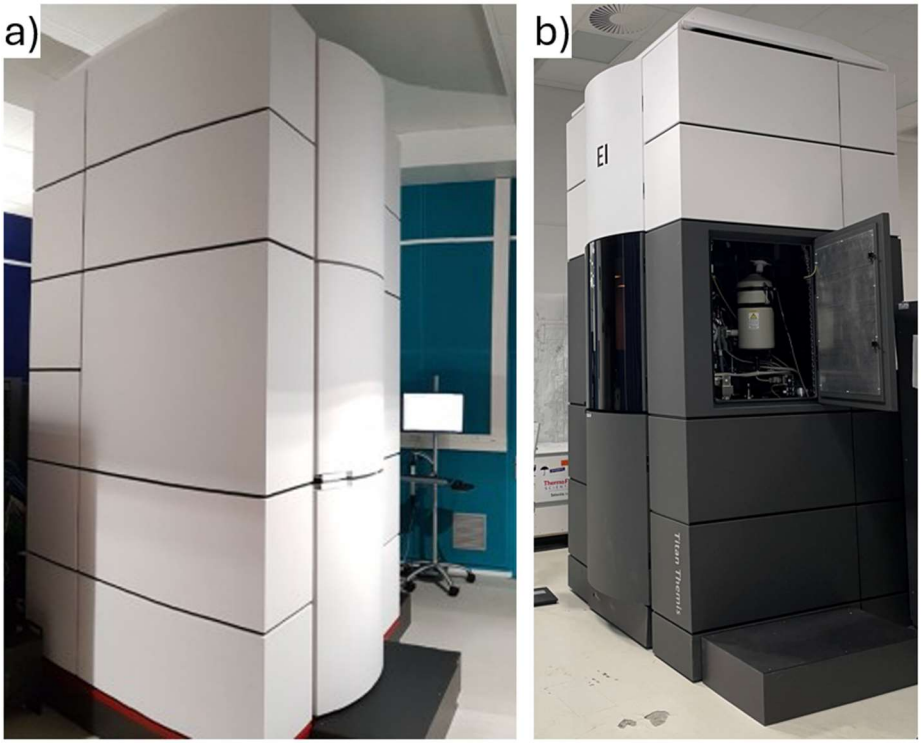

Figure 5. (Scanning) Transmission Electron Microscope a) "Nan'Themis", at the Institut des Matériaux de Nantes Jean Rouxel (IMN) in Nantes b) Iliad in Eindhoven at Thermo Fisher Scientific

Damage experiments on battery materials

5 Damage mitigation in beam sensitive solid battery material LiF with alternative scan patterns

In this chapter electron beam-induced damage will be investigated for LiF thin films with both HAADF and EELS experiments and mitigated using alternative scan patterns. The interleaved scan patterns, introduced in Chapter 4, are based on raster and snake scans, and were designed to achieve more homogeneous fluence distribution in subscans within the constraints of our scan engine. These alternative patterns are experimentally compared to conventional raster scan for their efficiency in mitigating beam damage.

5.1 HAADF studies on damage mitigation with scan patterns

5.1.1 Experimental approach

The influence of spatio-temporal fluence distribution on damage in LiF is experimentally examined through STEM-HAADF experiments with systematic variation of scan pattern, probe spacing, and probe flux. Damage is quantified by radiation-induced mass loss via HAADF intensity differences and analyzed across varying probe spacing, probe flux and two substrates of varying conductivity to understand the role of insulating environments. Our results reveal that interleaved raster scan consistently results in slower damage and reduced charging effects compared to conventional raster scan, that increasing probe spacing reduces damage, and probe flux effects are scan-pattern-dependent, with higher flux decreasing damage for interleaved scans but increasing it for conventional raster scans.

In these experiments a polycrystalline LiF sample deposited on silicon nitride and silicon dioxide were used (see Chapter 3 for details).

An overview of the measurement conditions is given in Table 2. The applied probe currents are 30pA, 60pA, 90pA and 120pA. The applied probe spacings are 1.6nm, 2.3nm, 3.2nm and 6.4nm, with 128x128 pixels (exception of 64 x 64 pixels for 6.4nm probe spacing) and a fixed dwell time of 100µs. The applied scan patterns are conventional raster scan (CRS), interleaved raster scan (IRS). In some experiments CRS is additionally compared to a rotated interleaved snake scan (RISS) and in a single experiment to a rotated interleaved Hilbert scan (RIHS).

Table 2. Overview of measurement conditions for HAADF damage experiments on LiF.

	Beam current (pA)	Dwell time (ms)	Number of pixels	Probe spacing (nm)	Cumulative fluence per frame from probe size (10^6 e$^-$Å^{-2})	Cumulative fluence per frame from pixel size (10^3 e$^-$Å^{-2})	pixel area to probe area ratio
LiF on Si_xN_y	30	0.1	128x128	1.6	0.037	0.072	520
	60	0.1	128x128	1.6	0.075	0.143	520
	90	0.1	128x128	1.6	0.112	0.215	520
	90	0.1	128x128	2.3	0.112	0.108	1039
	90	0.1	128x128	3.2	0.112	0.054	2075
	90	0.1	64x64	6.4	0.112	0.013	8299
	120	0.1	128x128	1.6	0.149	0.287	520
LiF on SiO_2	60	0.1	128x128	1.6	0.075	0.143	520
	90	0.1	128x128	1.6	0.112	0.215	520

For measurements with LiF on silicon oxide substrate, a drift correction was additionally applied, due to heavy drift in the first frames. The application of a drift correction led to prolonged acquisition times

for the same number of frames (see Chapter 4.3.3 for more details on scan time differences in experiments).

5.1.2 Data analysis

As a method to monitor induced damage, HAADF image series were acquired. Damage induced mass loss is correlated to the observed HAADF intensity decay. Exemplary HAADF image series for conventional and interleaved raster scan are displayed in Figure 53 to illustrate the damage assessment. In this particular example, observed mass loss is slower for interleaved raster scan (see Figure 53b) compared to conventional raster scan (see Figure 53a). For interleaved raster scans mass is preserved over a larger number of frames and a higher cumulative fluence compared to conventional raster scan. This observation needs to be quantified properly so that damage can be rigorously compared as a function of conditions applied.

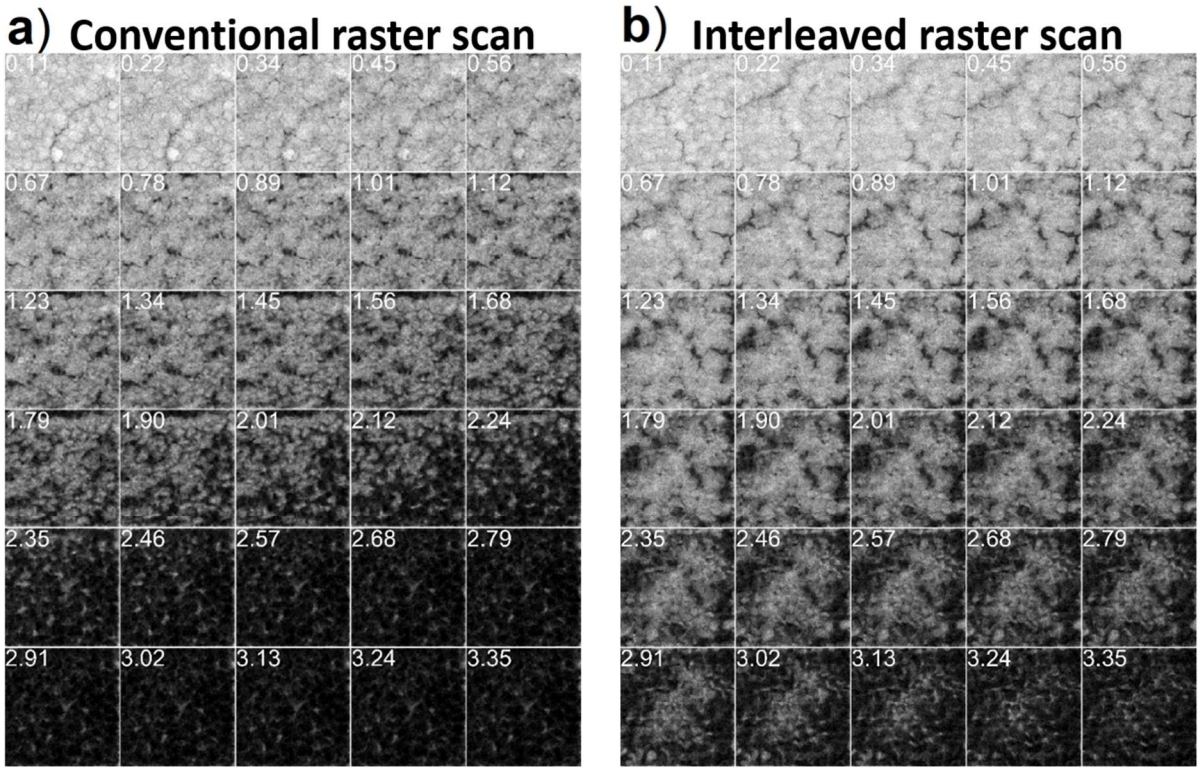

Figure 53. LiF on silicon nitride membrane imaged over several frames with a HAADF detector; increasing cumulative fluence denoted in upper left corner of frames (10^6 $e^-/Å^2$) with a) conventional raster scan and b) interleaved raster scan.

The necessary data treatment of an HAADF image series on LiF on a continuous substrate of silicon nitride (see Chapter 3 Choice of material and sample preparation for details on sample choice and preparation) is taken as an example and detailed in the following.

5.1.2.1 Data pretreatment: pixel subtraction, background subtraction, normalization

Given the large number of experiments, data analysis was automated using Python scripts. In a first step the first four pixel columns on the left hand side were removed from each image. This step is necessary because in the image series acquisition no flyback time is applied. Consequently, the first pixel of the subsequent line will include the intensity during its jump to the line start (see schematic probe path in Figure 52 in Chapter 4). For interleaved raster scan the flyback pixels are spread over the first four columns (see Figure 54a) due to the interleaving of 16 sparse subscans and therefor the first four columns are excluded from further analysis. For conventional raster scan cutting the first line would be sufficient and for the rotated interleaved snake pattern and the rotated interleaved Hilbert

scan no large jump distances are applied at all. However, to ensure that data analyses contain the same number of pixels and avoid bias in data processing, the first four pixel columns are systematically.

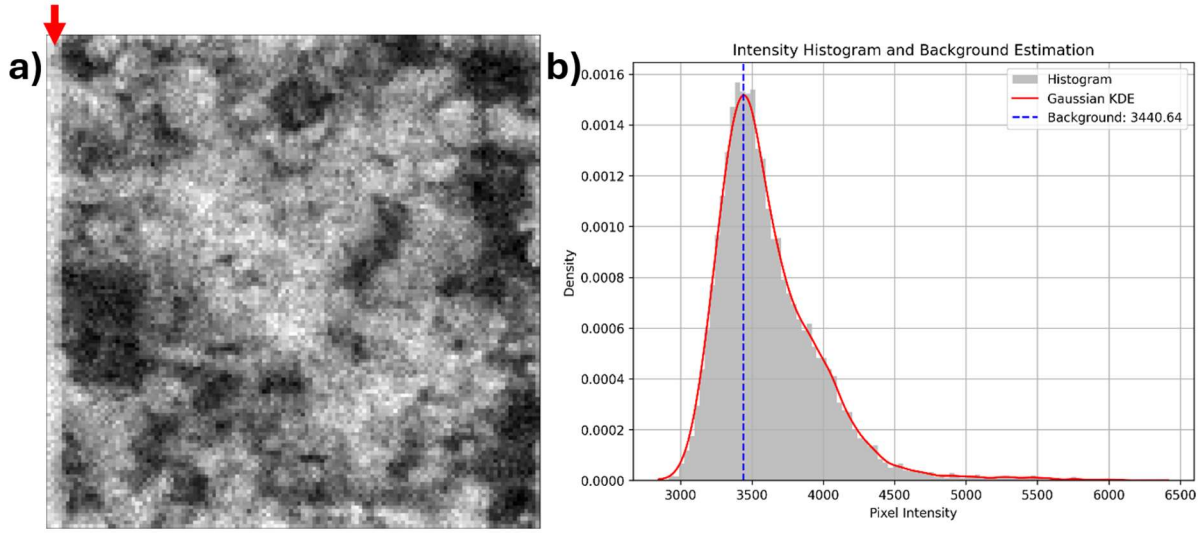

Figure 54. a) Exemplary HAADF frame acquired with interleaved raster scan, with first 4 columns of pixels (see red arrow) inherently including intensity from line flyback and b) histogram of intensity distribution of a frame at the end of the damage experiment with residue material on the substrate and a Gaussian KDE fit to determine the background intensity.

In a second step, background is subtracted. The thin films are sputtered onto a substrate. In some cases, a small amount of residue remained on the substrate even after prolonged irradiation. Therefore, the background intensity could not be determined by the mean intensity of the last frames. Instead, the main background intensity was determined by applying a Gaussian Kernel Density Estimate (KDE) fit on the histogram of the last frames of the damage series, which identifies the most frequent low-intensity value of the smoothed histogram. The final estimated background intensity to be subtracted from the image series is determined by taking the mean of the main background intensity found in the last 10 frames. In these last 10 frames usually no changes in intensity were observed and 10 frames is just an arbitrarily number of frames chosen to reduce noise or outliers in this background estimation step Next the mean frame intensity and their standard deviation is determined for each frame and the image series is normalized by dividing by the mean intensity of the first frame.

In Figure 55a) the normalized mean frame intensity decay is plotted versus cumulative fluence for each of the two scan pattern examples displayed in Figure 53. Here again slower intensity decay is observed for interleaved raster scan in light blue compared to conventional raster scan in dark blue.

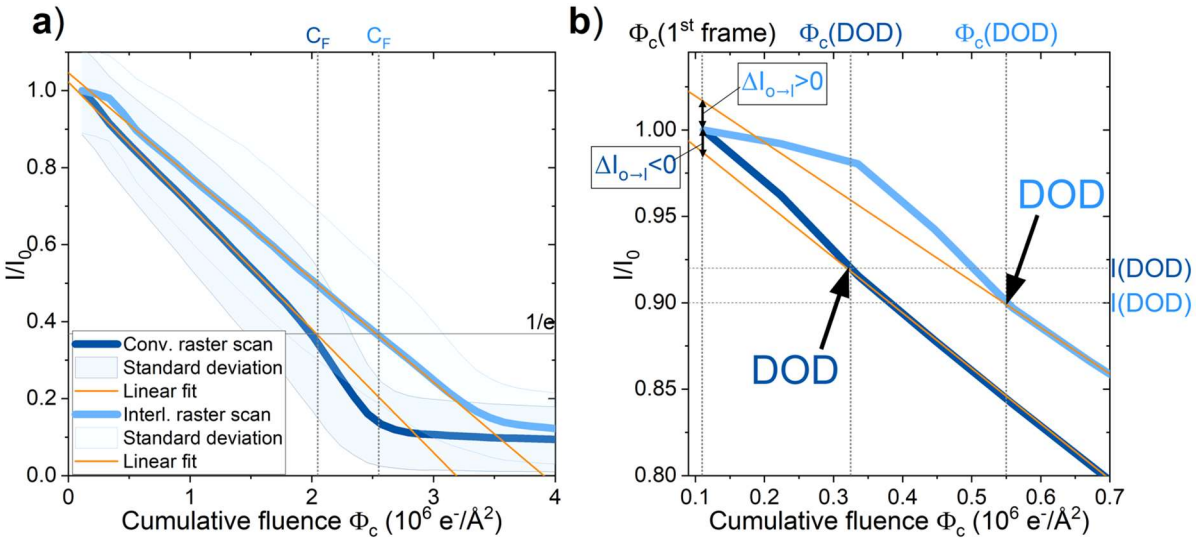

Figure 55. a) Normalized mean frame HAADF intensity decay for cumulative fluence compared for conventional raster (see image series in Figure 53a) and interleaved raster scan (see image series in Figure 53b); b) Zoom on onset region of a) with damage onset decay point DOD at intensity I(DOD) and cumulative fluence Φ_c(DOD) and intensity shift of linear region by onset region $\Delta I_{o\rightarrow I}$.

For both scan patterns, the HAADF intensity decay follows a non-linear trend, transitioning from a short, non-linear onset decay to a main linear decay region (see Figure 55a). To quantify the damage observed in the evolution of mean intensity across the image series, the analysis focuses on two aspects: distinct points in the decay graph and intensity decay rates, which describe how rapidly the intensity diminishes per unit of cumulative fluence. The different magnitudes used are detailed below.

Across different experiments, the intensity decay consistently exhibits an initial plateau like slower decrease, followed by a sharper drop before stabilizing into a linear decay. The **damage onset decay** point, **DOD**, marks the transition between these two regions (see DODs marked exemplary for each scan pattern in Figure 55b). The DOD is defined by two distinct values:

- **Φ_c(DOD)**: the cumulative fluence at which the linear mass loss regime begins.
- **I(DOD)**: the intensity lost when the linear regime is reached.

Both, Φ_c(DOD) and I(DOD) are exemplarily displayed in Figure 55b for each scan pattern plot. While Φ_c(DOD) primarily corresponds to the plateau phase of the onset, I(DOD) predominantly influenced by the accelerated phase of the onset. Φ_c(DOD) and I(DOD) values are correlated by calculating the **mean intensity decay rate** for the **onset region**, $\mathbf{r_{onset}}$, with the derivative -dI/dΦc (Å²/e⁻), which quantifies the average rate of intensity loss per unit of cumulative fluence. It has to be pointed out that r_{onset} captures the average trend of the onset region and is only an estimate of the true onset intensity decay behavior.

To accurately identify the DOD, a rolling window linear regression method is applied. Starting from the beginning of the damage series, a linear fit is applied to a fixed window of data points, and the slope, intercept, and coefficient of determination (R^2) are calculated. The linear region is confirmed when subsequent windows yield R^2 values exceeding 0.99 and the standard deviation of the slopes remains below a predefined stability threshold. The mean intensity decay rate for the onset region is determined from overall intensity loss in the onset region (1-I(DOD)) per cumulative fluence imposed in the onset region (Φ_c(DOD)-Φ_c(1st frame)) (see Figure 55b).

The **critical fluence, C_F**, is additionally used to compare induced damage. In Figure 55a C_F is exemplarily displayed for each scan pattern. In literature C_F acts as a measure of material stability under electron

radiation in certain acquisition conditions, including beam diameter, acceleration voltage and sample thickness[1]. Higher C_F indicate prolonged stability of the irradiated sample in given specific conditions. C_F is defined as the fluence at which the initial intensity falls to 1/e [2] and is determined from a linear fit after the DOD in the main linear decay region (see Figure 55a)). Additionally, the **intensity decay rate for the linear region**, $\mathbf{r_{linear}}$, is determined by the slope of the linear fit.

In one specific case, only a linear region could be determined but not the DOD. Here the relative **shift of the linear region by the onset region** was used to compare intensity decay rates between onset and linear region. Both the shift in intensity $\Delta I_{o\rightarrow l}$ and in cumulative fluence $\Delta\Phi_{o\rightarrow l}$ can be determined (see Figure 55b). Positive shift values ($\Delta I_{o\rightarrow l}$ >0) indicate slower damage rates and negative shift values ($\Delta I_{o\rightarrow l}$ <0) indicate accelerated damage rates in the onset region compared to the linear region (see Figure 55b).

In the specific example given here in Figure 53 and Figure 55, interleaved raster scan (IRS) depicts larger C_F, an extended DOD and slower damage rates compared to conventional raster scan (CRS), indicating comparably slower damage.

In the following sections, the Φ_c(DOD) and C_F values between different scan patterns are compared by **relative increase** of values for interleaved scans compared CRS-values with the calculation of ((interl. scan - CRS) / CRS) x 100%. Intensity decay rates in onset and linear regions are compared each among different scan patterns with the **relative decrease** of values for interleaved scans compared to CRS values, indicating how much slower intensity decay rates of interleaved scans are compared to CRS damage rates. Intensity decay rates between onset and linear region are compared by their **relative difference** calculated with $((r_{onset}–r_{linear})/r_{linear})$ x100%, indicating how much slower (rel. diff > 0) or faster (rel. diff < 0) onset region damage rates are compared to linear region damage rates.

Experiments were repeated several times and C_F, DOD and intensity decay rates are determined. The mean values for each scan pattern are then compared.

5.1.2.2 Spatial damage distribution

To investigate how uniform damage progresses spatially, damage will be additionally compared with contour maps of the spatial distribution of C_F and line plots in both vertical and horizontal directions. For the spatial C_F maps, the images, after removing the first four pixel columns on the lefthand side (as described above) were used for further data treatment. The image was background corrected by subtracting at each pixel the mean of the 10 lowest intensity values. The images series was normalized by dividing each pixel by its intensity in the first frame. To reduce noise and the effect of increased damage rates at grain boundaries, the frames in the image series were binned in both x and y by 4x4 pixels from originally 128x128 pixels to 32x32 pixels. For each binned pixel its local C_F value was estimated by the cumulative fluence at which the initial intensity dropped to 1/e. The resulting contour plot gives an overview of local differences in C_F.

The damage series is further compared by line plots in both horizontal and vertical direction (see schematic example in Figure 56). To account for low signal to noise ratio, line scans were binned over 8x128 pixels, resulting in 16 binned line scans over the frame area. Comparing vertical and horizontal line scans give insights on intensity decay differences from left to right and top to bottom of the frame area respectively.

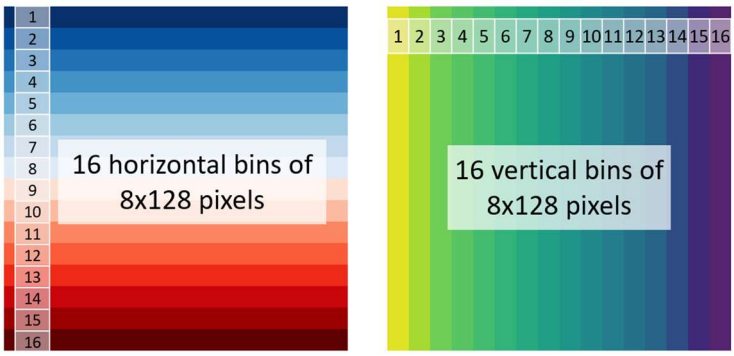

Figure 56. Schematic example for binning applied for vertical and horizontal line plots over a frame.

5.1.3 Results and discussion

5.1.3.1 Effect of probe spacing: raster vs. interleaved raster scan

To investigate the influence of probe spacing on the induced mass loss by conventional and interleaved raster scan, LiF on a silicon nitride membrane was exposed using each scan pattern for different probe spacing of 1.6, 2.3, 3.2 and 6.4nm. The normalized HAADF-STEM intensity decay for increasing cumulative fluences are shown in Figure 57. Measurements were reproduced 5 to 8 times for each probe spacing and scan pattern in different areas of the sample.

For each of these experiments the mean frame intensity evolution with increasing cumulative fluence is displayed in Figure 57 as scatter plots, along with line plots representing the average intensity decay for experiments with identical scan pattern and probe spacing. The critical fluence (C_F) and DOD values for the different probe spacings and for conventional raster scan (CRS) and interleaved raster scan (IRS) derived from the graphs in Figure 57 are plotted in Figure 58 and summarized in Table 3. An exemplary C_F map for each applied scan pattern and probe spacing is displayed in Figure 59.Additionally, intensity decay rates for the onset regions and linear regions, determined from the graphs in Figure 57 are summarized in Table 4.

The mean intensity decay graphs for different probe spacings and scan patterns (Figure 57), exhibit a consistent trend in intensity decays, with a non-linear onset region followed by a main linear region. Increased probe spacing results in an overall slower intensity decay. For example, at 6.4nm probe spacing the intensity decay is ranging to about 20 times the cumulative fluences compared to 1.6nm probe spacing (compare Fig 19 a and b abscissa). Scanning with IRS also leads to overall slower intensity decay compared to CRS (Fig 19a), though the effect is less pronounced than that of increased probe spacing (Fig 19d).

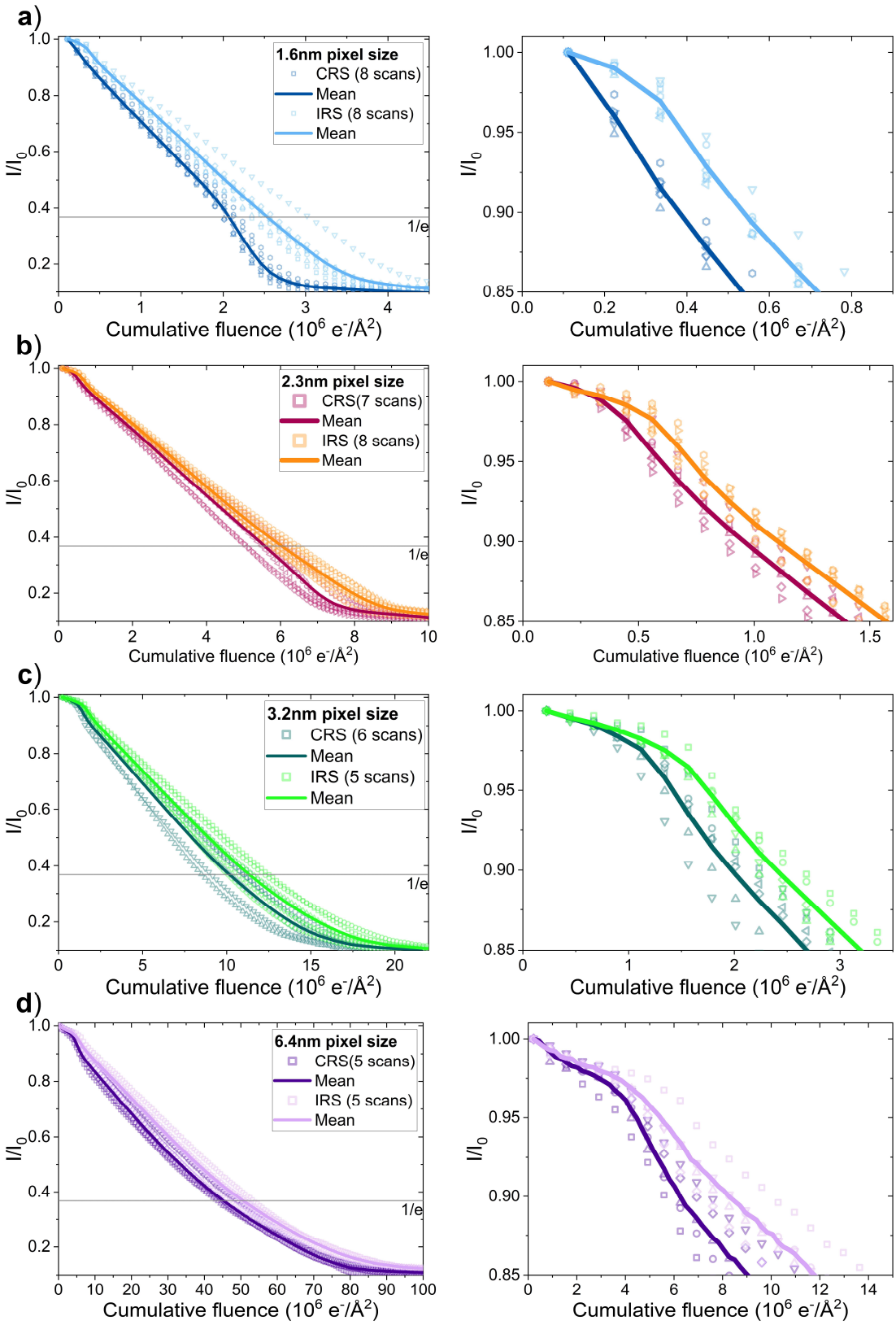

Figure 57. Normalized HAADF intensity decay versus cumulative fluence for conventional (CRS) and interleaved raster scan (IRS) comparing different pixel sizes of 1.6nm, 2.3nm, 3.2nm and 6.4nm for LiF on Si_xN_y substrate for a beam current of 90pA. Single intensity decay series are plotted with number of measurements per pixel size and scan pattern indicated in brackets in the legend and mean of single measurements plotted with a line.

To precisely quantify the observed damage, C_F values are determined from plots in Figure 57 and plotted in Figure 58a) and summarized in Table 3, for different probe spacings and scan patterns.

Increasing the probe spacing leads to larger C_F values, indicating reduced radiation damage. For CRS at 1.6nm C_F is 2.1±0.1 x 10^6 $e^-/Å^2$ increasing with larger probe spacings up to 40.2±4.2 x 10^6 $e^-/Å^2$ at 6.4nm probe spacing. C_F values for IRS are consistently larger compared to CRS C_F values, with C_F ranging from 2.6±0.2 x 10^6 $e^-/Å^2$ at 1.6nm probe spacing to 46.2±3.3 x 10^6 $e^-/Å^2$ at 6.4nm probe spacing. The relative increase of the C_F-values for interleaved compared to conventional raster scan is highest at 1.6 nm (20%), lowest at 2.3nm (7%), and increased again at 3.2 nm (11%) and 6.4 nm (15%), with a similar trend observed for intensity decay rates. Therefore, the efficiency of interleaved raster to slow damage does not show a monotonic trend. However, it has to be noted that all the C_F values for the two different scan patterns at the same probe spacing are within their standard deviation, except the measurement at 1.6nm probe spacing.

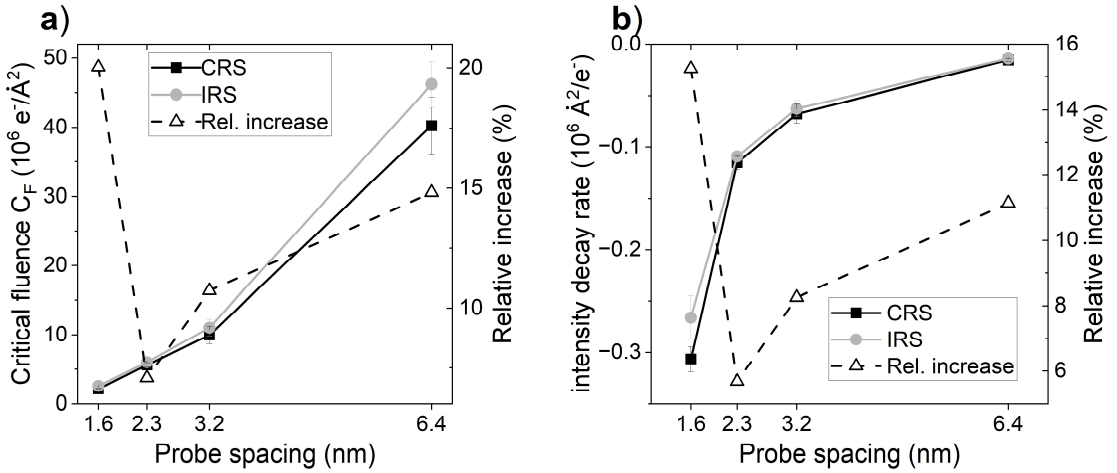

Figure 58. a) Critical fluence C_F and b) intensity decay rate for linear region for different probe spacings and scan patterns; CRS: conventional raster scan, IRS: interleaved raster scan; relative increase indicating relative increase of IRS values compared to CRS values.

In Figure 59 C_F maps for different probe spacings and scan patterns are displayed. CRS and IRS are plotted with the same cumulative fluence scale for each probe spacing respectively. For IRS the intensities in the frame show higher cumulative fluences compared to CRS (overall brighter colors), indicating slower damage. Spatio-temporal damage distribution is relatively uniform in most of the different experiments. By comparison with initial HAADF images, the mass loss appears to be accelerated at grain boundaries (darker C_F). In Figure 60 this is exemplarily displayed in a direct comparison of HAADF images at different cumulative fluences and a C_F-map, where accelerated mass loss at grain boundaries is marked with arrows. The example given in Figure 60 correlates to the C_F-map in Figure 59 for IRS at 1.6nm probe spacing, but here pixels were not binned for better comparability with HAADF frames and better display of grain boundary effects. In Figure 59, for the C_F-map of CRS at 1.6nm a slight tendency for accelerated damage in the lower right part of the frame is observed (darker contrast), which will be further discussed later on in the following sections. For the 3.2 nm spacing, large trenches are visible dividing the whole frame, which can be associated to cracks that formed early on in the damage experiment. These cracks were mostly observed for the experiments on this measurement day and did not appear for other probe spacings. As here area is divided by the trench, slight differences in damage dynamics can be expected, compared to other scan patterns.

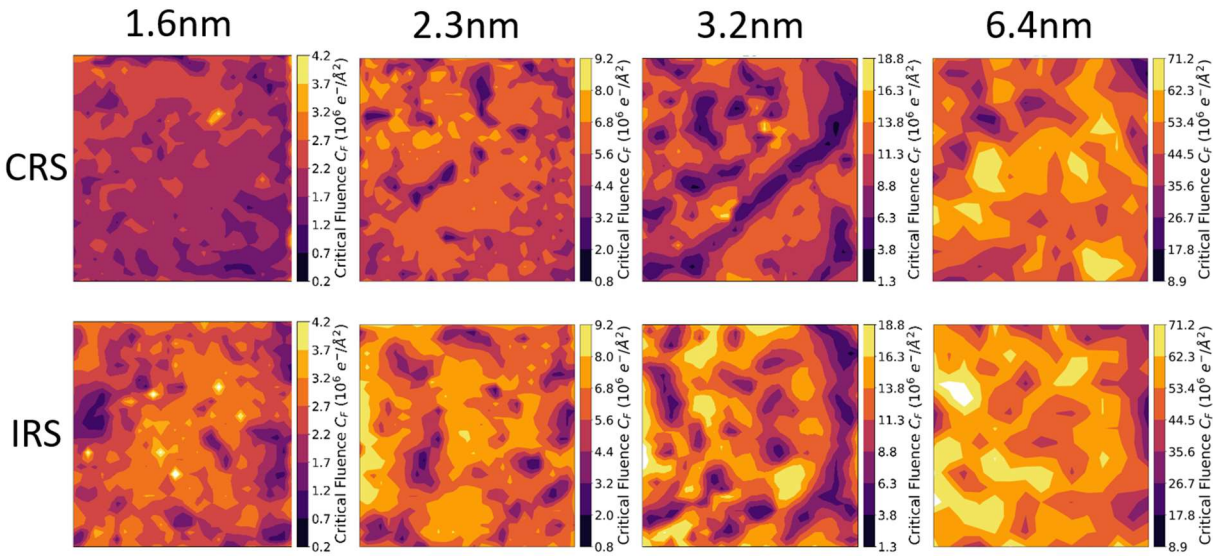

Figure 59. C_F maps for different scan patterns and probe spacings.

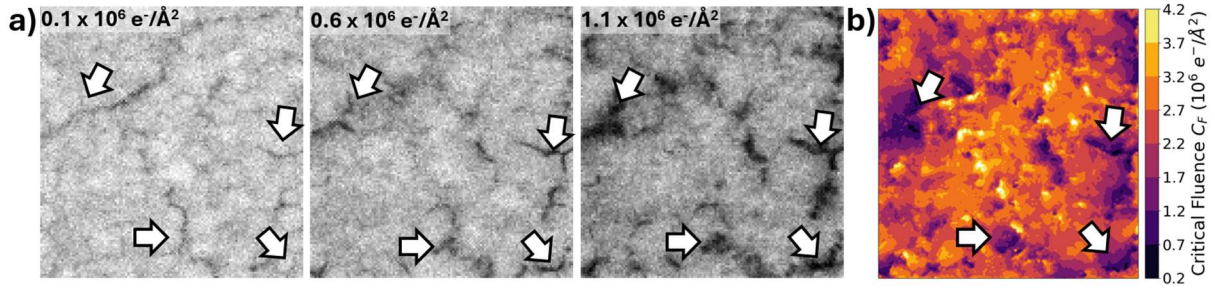

Figure 60. Preferential damage at grain boundaries exemplarily displayed for a) three HAADF frames in a damage series at different cumulative fluences and b) for a C_F-map of the same experiment as in a); here the C_F-map is displayed without binning pixel areas to better display accelerated damage at grain boundaries.

To investigate differences in the damage behavior at the beginning of the damage series, we will first concentrate on mean DOD values determined from the single experiments displayed Figure 57, for each probe spacing and scan pattern. The mean DOD values, consisting of I(DOD) and Φ_C(DOD), which are defined as the as the intensity and the cumulative fluence at which DOD ends, are plotted in Figure 61 and listed in Table 3. The cumulative fluence extend of the onset region Φ_C(DOD) increases with larger probe spacings, independent of the scan pattern (see Figure 61a and c). The Φ_C(DOD) values for IRS are larger compared to CRS. The relative increase of the Φ_C(DOD) values for IRS compared to CRS is highest at 1.6 nm (105%) and decreasing with larger probe spacings (35% at 2.3 nm, 15% at 3.2 nm and 7% at 6.4 nm). However, for the values at 3.2nm and 6.4nm the standard deviation of Φ_C(DOD) for the two scan patterns overlapped (see Table 3) and for lower probe spacings the decreased number of measurement points in the onset region (see onset region in Figure 57) probably also decrease the accuracy of Φ_C(DOD). Additionally, it has to be considered that even though Φ_C(DOD) is larger for IRS (see Figure 61 a and c), the corresponding intensity loss I(DOD) is only smaller for IRS for 3.2 and 6.4nm probe spacing and larger for 1.6 and 2.3nm probe spacing (see Figure 61 a and b). To get a better overview of the intensity loss per fluence in the onset region, mean intensity decay rate values for the onset region, r_{onset}, are determined and listed in Table 4. The r_{onset}-values are decreasing with increasing probe spacing, independent of the applied scan pattern. As can be seen in Table 4 in the column for r_{onset}, overall slower intensity decay rates in the onset region are obtained for IRS compared to CRS. The efficiency of IRS to slow the intensity decay in the onset region is highest at 1.6 nm (47%), lowest at 2.3 nm (18%), and increased again at 3.2 nm (23%) and 6.4 nm (30%) (see rel. decr. in column of r_{onset} in Table 4).

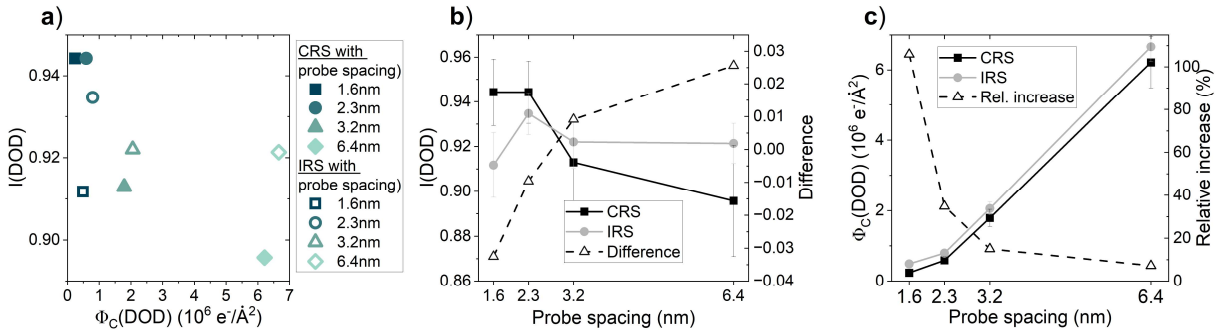

Figure 61. DOD values for different probe spacings and scan patterns; a) Intensity at end of onset region I(DOD) versus cumulative fluence at the end of onset Φ_c(DOD); b) I(DOD) for different probe spacings; c) Φ_c(DOD) for different probe spacings; CRS: conventional raster scan; IRS: interleaved raster scan.

Table 3. Critical Fluence C_F and DOD for different probe spacings d and scan patterns.

d	C_F 10^6 e$^-$/Å^2			I(DOD)			Φ_C(DOD) 10^6 e$^-$/Å^2		
(nm)	CRS	IRS	Rel. incr.	CRS	IRS	Δ	CRS	IRS	Rel. incr.
1.6	2.1±0.1	2.6±0.2	20%	0.06±0.01	0.09±0.01	0.03	0.24±0.04	0.49±0.06	106%
2.3	5.6±0.3	6.0±0.3	7%	0.06±0.01	0.07±0.01	0.01	0.59±0.11	0.80±0.07	35%
3.2	10.0±1.3	11.0±1.2	11%	0.09±0.02	0.08±0.01	-0.01	1.79±0.24	2.06±0.19	15%
6.4	40.2±4.2	46.2±3.3	15%	0.10±0.02	0.08±0.01	-0.03	6.21±0.73	6.66±0.43	7%

I(DOD): DOD intensity, Φ_C(DOD): cumulative fluence at DOD, CRS: conventional raster scan, IRS: interleaved raster scan, rel. incr.: relative increase of IRS compared to CRS; Δ: absolute difference between CRS and IRS values; all measurements are on LiF on Si_xN_y with 90pA beam current.

Table 4. Intensity decay rate for DOD and linear region for different probe spacing d and scan patterns.

d	Intensity decay rates r_{onset} (10^{-6} Å^2/e$^-$)			r_{linear} (10^{-6} Å^2/e$^-$)			Relative difference onset versus linear region	
(nm)	CRS	IRS	Rel. decr.	CRS	IRS	Rel. decr.	CRS	IRS
1.6	0.443	0.230	47%	0.306	0.266	13%	-45%	+12%
2.3	0.116	0.095	18%	0.115	0.109	5%	-1%	+13%
3.2	0.052	0.040	23%	0.068	0.062	8%	+23%	+36%
6.4	0.017	0.012	30%	0.016	0.014	10%	-9%	+15%

CRS: conventional raster scan, IRS: interleaved raster scan, rel. decr.: relative decrease of IRS values compared to CRS values, indicating how much slower IRS damage rates are compared to CRS damage rates; rel. diff. onset vs. linear region CRS or IRS relative difference of intensity decay rate in onset versus linear region ($(r_{onset}-r_{linear})/r_{linear}$) for CRS and IRS respectively, indicating how much slower (rel. diff > 0) or faster (rel. diff < 0) onset region damage rates are compared to linear region damage rates; all measurements are on LiF on Si_xN_y with 90pA beam current.

The linear region after the DOD point is now examined. (see Figure 58b) and Table 4). The damage trends for the different probe spacings and scan patterns are similar to the trends observed for C_F, as C_F is mainly determined from the linear region of the HAADF intensity decay.

The last two columns in Table 4 compare the intensity decay rates for onset (r_{onset}) and linear (r_{linear}) region for each scan pattern. Once again, here r_{onset} is an average value of the intensity decay rate in the onset region and can only give an approximation of the overall intensity decay in this region combining the impact of I(DOD) and Φ_C(DOD), while above the trends for the extend of the plateau region were approximated with Φ_C(DOD). For IRS, the average intensity decay rate in the onset region (r_{onset}) is consistently slower compared to the following linear region (r_{linear}). For CRS on the other hand, the onset region shows faster intensity decay rates at 1.6nm (45% faster) and 6.4 nm (9% faster), comparable decay rates at 2.3 nm (1% faster) and slower at 3.2nm (23% slower). The comparably slower onset region for 3.2nm probe spacing could result from the sample region chosen for this

experiment, which formed large cracks over the whole frame within the first frame exposition. These large cracks could potentially slow the damage in the onset region.

As mentioned above, an effect of beam separation in STEM-EELS has been observed for beam sensitive materials, thus demonstrating a delocalization of damage [2–4]. For highly focused probes, it has been proposed that inelastic scattering, secondary beam-matter interactions, diffusing damage species and charging effects are delocalized, extending beyond the probe position [5]. In a semi empirical model it has been proposed that for raster scanning, damage volumes from adjacent pixels overlap, accelerating cumulative damage [6]. Increasing probe spacing can be used as a strategy to mitigate damage, however, it compromises spatial resolution, creating a trade-off between damage mitigation and resolution [3]. It has to be noted that even in the case of a true raster scan where the probe is accelerated to a constant velocity in each line (opposed to the here applied leapfrog scan where the probe is parked in the center of each pixel location, see Chapter 4 Scan engine control and scan pattern design for more details), a spacing of the probe will still be found in the slower scan direction (i.e. between each scan lines in conventional raster scan), and thus this is an effect worth studying. As mentioned previously, interleaved scanning is an approach to reduce damage without sacrificing resolution, by delaying the scanning of nearest neighbor pixels and provides additional time for defect recombination and relaxation compared to CRS where immediate irradiation of nearest neighbor pixels, promotes fast accumulation of damage defects [6,7]. While theoretical models support this approach [6,8,9], experimental validation remains limited. Notably, Velazco et al. demonstrated an 11% reduction in mass loss for atomic-resolution imaging of zeolite samples using their interleaved scan pattern [7]. Although no information is given on the degradation mechanisms involved in these porous materials, they are most likely different from those at work in LiF thin films where Li metal can be produced. LiF, also prone to radiolysis-induced mass loss is complementary to this previous study. The equilibrium between defect creation and recombination in LiF may compete with defect agglomeration and diffusion of fluorine species to surfaces and grain boundaries. Both depend on the mobility of defects (DH>>DF [10,11]), which again depends on radiation enhanced diffusion and therefore defect density [12].

The observed damage behavior in LiF under electron irradiation can be explained by considering the kinetics of defect formation and evolution. Two distinct damage regimes are observed. In the onset region, an intensity plateau is typically followed by an accelerating intensity loss until finally a linear intensity loss regime is reached. This implies a buildup process in the onset region followed by a steady state condition in the linear region. In literature for LiF, defect evolution is described with a rise in F and H-defects followed by diffusion assisted agglomeration of defects. In the onset region, defect concentrations (F- and H-centers) are likely still increasing toward saturation. H-center saturation concentration is reached faster than for F-centers, due to their larger mobility [10]. In the linear decay region, steady-state conditions are likely established where F- and H-center concentrations have reached saturation, and mass loss is limited by defect diffusion [10,13].

Consistent with literature observations, damage is slower with increasing probe spacing for both scan patterns, as evidenced by higher C_F values, extended Φ_C(DOD) and lower mass loss rates. This is consistent with our observations in monochromated STEM-EELS experiments (see Chapter 2.12), where increased probe spacing slowed the accumulation of defects and delayed metallic Li formation.

IRS consistently exhibits higher C_F values resulting from both, extended Φ_C(DOD) and slower intensity decay rates than CRS, indicating reduced damage for all applied probe spacings.

For IRS, Φ_C(DOD) is extended to higher cumulative fluences compared to CRS (see Figure 61 and Table 3) and IRS shows slower mean intensity decay rates in the onset compared to CRS (see Table 4). IRS

does not only delay reaching steady state intensity loss conditions to higher cumulative fluences but also shows slower mass loss rates during the buildup of F and H defect concentrations towards saturation concentration compared to CRS. Additionally, for IRS, the intensity decay rate for the linear region r_{linear} is slower compared to CRS (see r_{linear} in Table 4). Differences in the observed damage for the two scan patterns likely have similar origins to that for increased probe spacing, since IRS can be viewed as an initial sparser scan that becomes denser with time. Scanning with sparse subscans compared to dense scanning of immediate scan points, mitigates damage by reducing influence of neighboring pixel by allowing for relaxation of delocalized species by a temporal delay. This might help for the onset region by delaying H and F center saturation concentrations to higher cumulative fluences and for the linear region by delaying agglomeration of defects. However, this effect is limited as still the same number of pixels and the same fluence is introduced to the sample for both IRS and CRS.

The two scan patterns showed different trends when comparing the averaged intensity decay rate in the onset region, r_{onset}, compared to the intensity decay rate in the linear region, r_{linear}. For CRS, r_{onset} was faster compared to r_{linear} (except for 3.2 nm probe spacing) while for IRS average mass loss is slower in the onset region compared to its following linear region. It has to be kept in mind that r_{onset} is only approximating overall intensity decay rate in the onset region by an average, while the onset region actually consists of a plateau followed by an accelerated region. For CRS (with $r_{onset}>r_{linear}$) the onset region seems to be dominated by the accelerated part of the onset region, while for IRS (with $r_{onset}<r_{linear}$) the plateau region is the more prominent part of the onset region. This observed trend might be explained with the differences in F and H center concentration evolution before saturation concentrations are reached. H center saturation concentrations are reached almost instantaneous compared to F-centers concentrations, which have been reported to increase slower towards saturation concentrations [10]. The slower buildup of F-center concentrations limiting effective recombination might enhance H mobility during the onset and in combination with the dense scan point density induced by CRS, radiation enhanced diffusion might be accelerating H center diffusion to the surface more effectively compared to IRS.

The efficiency of IRS to mitigate damage compared to CRS, indicated by the relative increase of intensity decay rates and C_F, is showing a nonlinear trend with increasing probe spacings (see relative increase in Figure 58a) and b), rel. incr. of C_F in Table 3 and rel. decr. of r_{onset} and r_{linear} in Table 4). The effect of IRS to mitigate damage compared to CRS is highest at 1.6nm and 6.4nm and lowest at 2.3nm and suggests a complex interplay between spatial and temporal factors. This behavior may be related to the spontaneous recombination distance of F-H pairs estimated to be 5-10 lattice sites in Alkali Halides [14,15]. For LiF this is approximately 1.4-2.8 nm. The 2.3 nm probe spacing may represent a critical transition point where the balance between recombination and diffusion processes changes. At 1.6nm, larger mass loss rates are observed for conventional raster scan. Large density of defects increases radiation enhanced diffusion and mass loss by diffusion of H-centers and agglomeration of defects is probably favored over recombination. Interleaved raster scan reduces the spatio–temporal density of defects reducing radiation enhanced diffusion and agglomeration. At 3.2nm and 6.4nm, probe spacing exceeds the recombination distance of F-H pairs. The sparser nature of the scan positions reduces defect densities and probability for agglomeration. Reduced defect densities at increased probe spacing make recombination of defects dependent on defect diffusion. The delay of imaging pixels at proximity, introduced by interleaved raster scanning, allows for diffusion assisted recombination. At 2.3nm, probe spacing might match the maximum recombination distance and spatio-temporal separation of nearest neighbor positions introduced by the interleaved raster, and IRS cannot fully overcome the competing recombination and agglomeration processes.

5.1.3.2 *Investigating effect of probe spacing with averaged frame fluence*

In some damage studies, the fluence is calculated with the pixel area instead of the probe area. Here, pixel area is significantly larger compared to probe area (see Table 2 for ratios of probe area to pixel area ranging from 520 to 8300). Calculating fluence with pixel area would underestimate the actual electron density in the probe by a large factor. However, above, it was shown that damage spreads far beyond its probe area. As an approach to account for different amounts of sample area, the fluence is introduced to and spread over by different pixel spacings, here, the same experiments as above are displayed with fluence calculated by square pixel area, which effectively describes the averaged distribution of electron fluence in the frame. This rescaling of the applied fluence will not change any intensity values or the relative difference between scan patterns to the evaluation above and will therefore not further be commented here.

In Figure 62 the normalized mean frame intensity decay is plotted for increasing cumulative pixel fluence for different probe spacings and scan patterns. Compared to the related probe fluence experiments (see Figure 57), the intensity decays for different probe spacings spread here over a quite similar cumulative pixel fluences range, which is approximately three orders of magnitude smaller compared to the probe fluence. This trend is also reflected for the C_F values (determined from plots in Figure 62) which are plotted in Figure 63a) and summarized in Table 5 (for equivalent experiments with probe fluence see Figure 58 and Table 3). C_F-values are relatively similar, ranging from 4.1 x 10^3 $e^-/Å^2$ to 5.9 x 10^3 $e^-/Å^2$, with lowest C_F at 1.6nm probe spacing, highest at 2.3nm probe spacing and intermediate C_F values at 3.2nm and 6.4nm probe spacing. However, most of the CF values are within their error range, with the exception of the two lowest probe spacings for CRS.

The DOD values for different probe spacings and scan patterns are plotted in Figure 64 and summarized in Table 5. For CRS, the extend of Φ_C(DOD) is increasing with the probe spacing and similar values are obtained at 3.2 and 6.4nm. For IRS Φ_C(DOD) values are relatively similar over the different probe spacings ranging from 0.77 x 10^3 $e^-/Å^2$ at 2.3nm probe spacing to 0.99 x 10^3 $e^-/Å^2$ at 3.2nm probe spacing.

Table 5. Critical Fluence CF and DOD for different probe spacings d and scan patterns.

d	C_F 10^3 $e^-/Å^2$		I(DOD)		Φ_C(DOD) 10^3 $e^-/Å^2$	
(nm)	CRS	IRS	CRS	IRS	CRS	IRS
1.6	4.08±0.18	4.90±0.39	0.06±0.01	0.09±0.01	0.46±0.08	0.94±0.11
2.3	5.39±0.32	5.77±0.25	0.06±0.01	0.07±0.01	0.57±0.10	0.77±0.07
3.2	4.81±0.60	5.32±0.58	0.09±0.02	0.08±0.01	0.86±0.12	0.99±0.09
6.4	4.85±0.50	5.57±0.40	0.10±0.02	0.08±0.01	0.75±0.09	0.80±0.05

I(DOD): DOD intensity, Φ_C(DOD): cumulative fluence at DOD, CRS: conventional raster scan, IRS: interleaved raster scan; all measurements are on LiF on Si_xN_y with 90pA beam current.

The intensity decay rates for onset r_{onset} and linear r_{linear} region are plotted for different probe spacings and scan patterns in Figure 63b) and summarized in Table 6. The r_{onset} and r_{linear} values are relatively similar for probe spacings of 2.3nm, 3.2nm and 6.4nm, while r_{onset} and r_{linear} are larger for 1.6nm probe spacing. For CRS at 1.6nm probe spacing r_{onset}= 0.23 x 10^{-3} $Å^2/e^-$ and r_{linear} = 0.16 x 10^{-3} $Å^2/e^-$, while for higher probe spacings r_{onset} is about 0.12 ± 0.01x 10^{-3} $Å^2/e^-$ and r_{linear} = 0.13 ± 0.01 x 10^{-3} $Å^2/e^-$. For IRS, at 1.6nm probe spacing r_{onset}= 0.12 x 10^{-3} $Å^2/e^-$ and r_{linear} = 0.14 x 10^{-3} $Å^2/e^-$, while for higher probe spacings r_{onset} is about 0.09 ± 0.01x 10^{-3} $Å^2/e^-$ and r_{linear} = 0.12 ± 0.01 x 10^{-3} $Å^2/e^-$

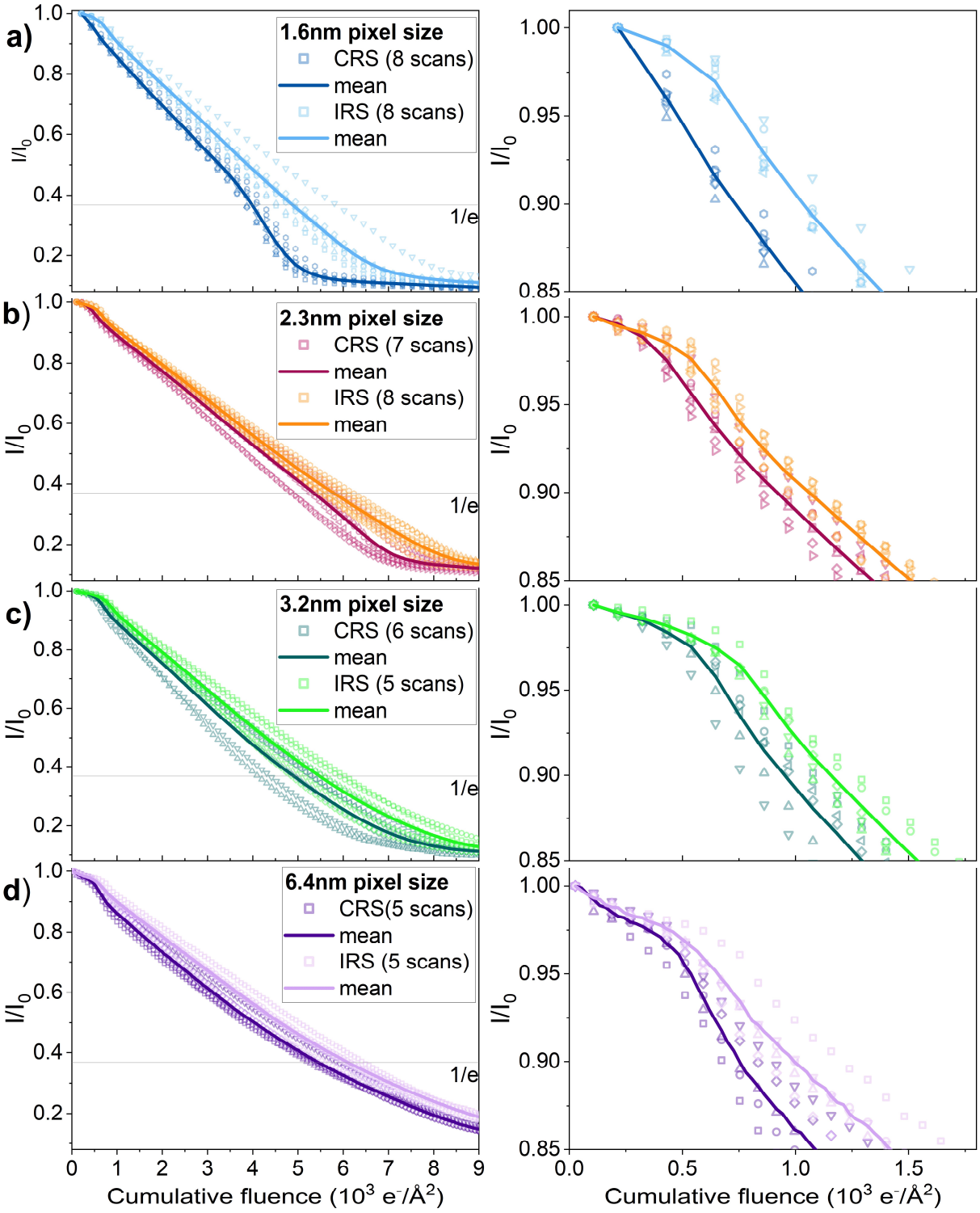

Figure 62. Normalized HAADF intensity decay versus cumulative pixel fluence for conventional (CRS) and interleaved raster scan (IRS) comparing different pixel sizes of 1.6nm, 2.3nm, 3.2nm and 6.4nm for LiF on Si_xN_y substrate for a beam current of 90pA. Single intensity decay series are plotted with number of measurements per pixel size and scan pattern indicated in brackets in the legend and mean of single measurements plotted with a line.

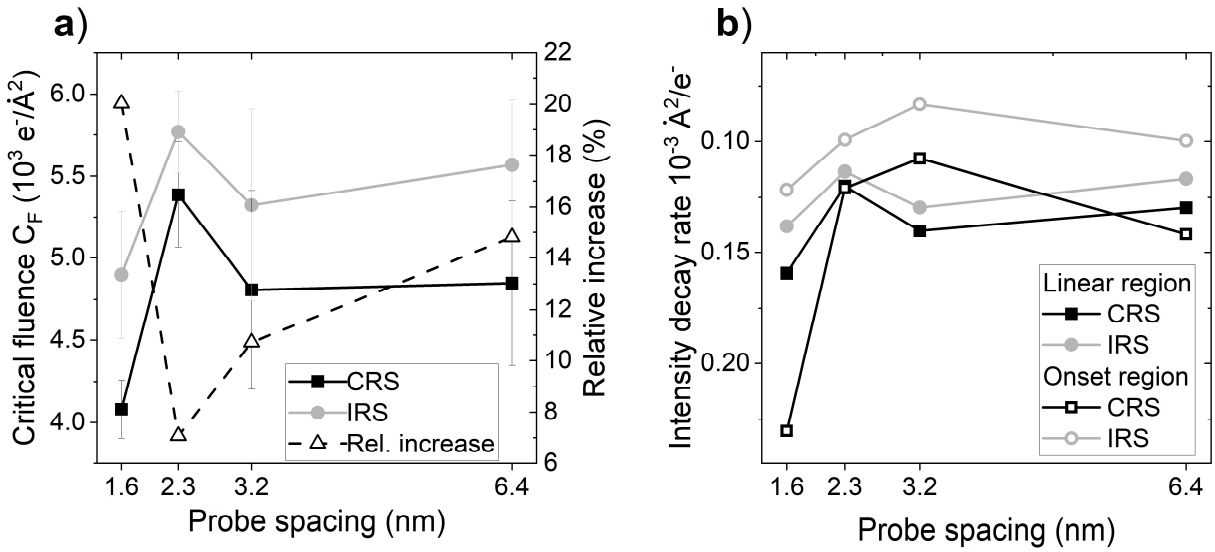

Figure 63 . a) Critical fluence C_F and b) intensity decay rate for linear region for different probe spacings and scan patterns; CRS: conventional raster scan, IRS: interleaved raster scan; relative increase indicating relative increase of IRS values compared to CRS values.

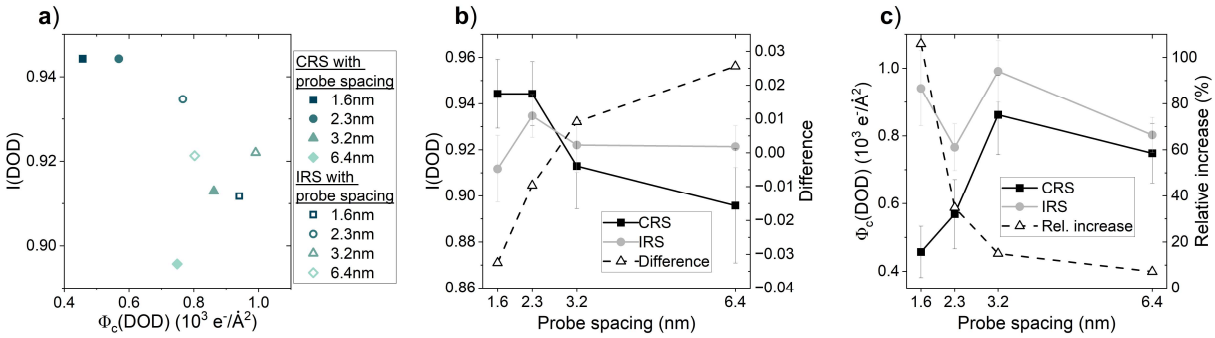

Figure 64. DOD values for different probe spacings and scan patterns; a) Intensity at end of onset region I(DOD) versus cumulative fluence at the end of onset Φ_c(DOD); b) I(DOD) for different probe spacings; c) Φ_c(DOD) for different probe spacings; CRS: conventional raster scan; IRS: interleaved raster scan.

Table 6. Intensity decay rate for onset region and linear region for different probe spacing d and scan patterns.

	Intensity decay rate			
d	Onset region (10^{-3} Å^2/e$^-$)		Linear region (10^{-3} Å^2/e$^-$)	
(nm)	**CRS**	**IRS**	**CRS**	**IRS**
1.6	0.230	0.122	0.159	0.138
2.3	0.121	0.099	0.120	0.114
3.2	0.108	0.083	0.140	0.130
6.4	0.141	0.100	0.130	0.117

CRS: conventional raster scan, IRS: interleaved raster scan; all measurements are on LiF on Si_xN_y with 90pA beam current.

Here for the investigation of probe spacing effects with the mean frame fluence (opposed to the probe fluence in the section before), overall, more similar damage is observed. The only exemption is the smallest probe spacing of 1.6nm where comparably faster damage is observed. Fluence calculated from the pixel area correlates the total fluence introduced at high density at each probe position to the total area in between all irradiated probe positions to an average frame fluence. Consequently, mean frame fluence decreases for increased probe spacing for the here applied case of constant probe fluence. The here observed trend (damage values calculated with the average frame fluence hardly change for most probe spacings), indicates that in these conditions the damage induced correlates with the amount of sample area in between irradiated probe positions, supporting delocalized damage spread far from initial probe position. The only exemption of larger damage at 1.6nm probe spacing

for CRS, supports the claims in previous section that there is a change in damage dynamics around 2.3nm probe spacing, below which damage is less diffusion based presumably due to higher fluence density, which can be avoided by IRS.

5.1.3.3 Influence of probe flux

To investigate the influence of probe flux on the resulting mass loss by conventional and by interleaved raster scans, LiF (on silicon nitride membrane) was imaged with each scan pattern four to eight times at different probe currents of 30pA, 60pA, 90pA and 120pA (see Figure 65). For interleaved raster scan, the decay of the normalized intensity as a function of cumulative fluence followed a similar trend consistent across all probe currents, exhibiting a short DOD followed by a linear decay. In contrast, for conventional raster scan, the intensity decay becomes nonlinear at higher cumulative fluences and even more with higher fluxes.

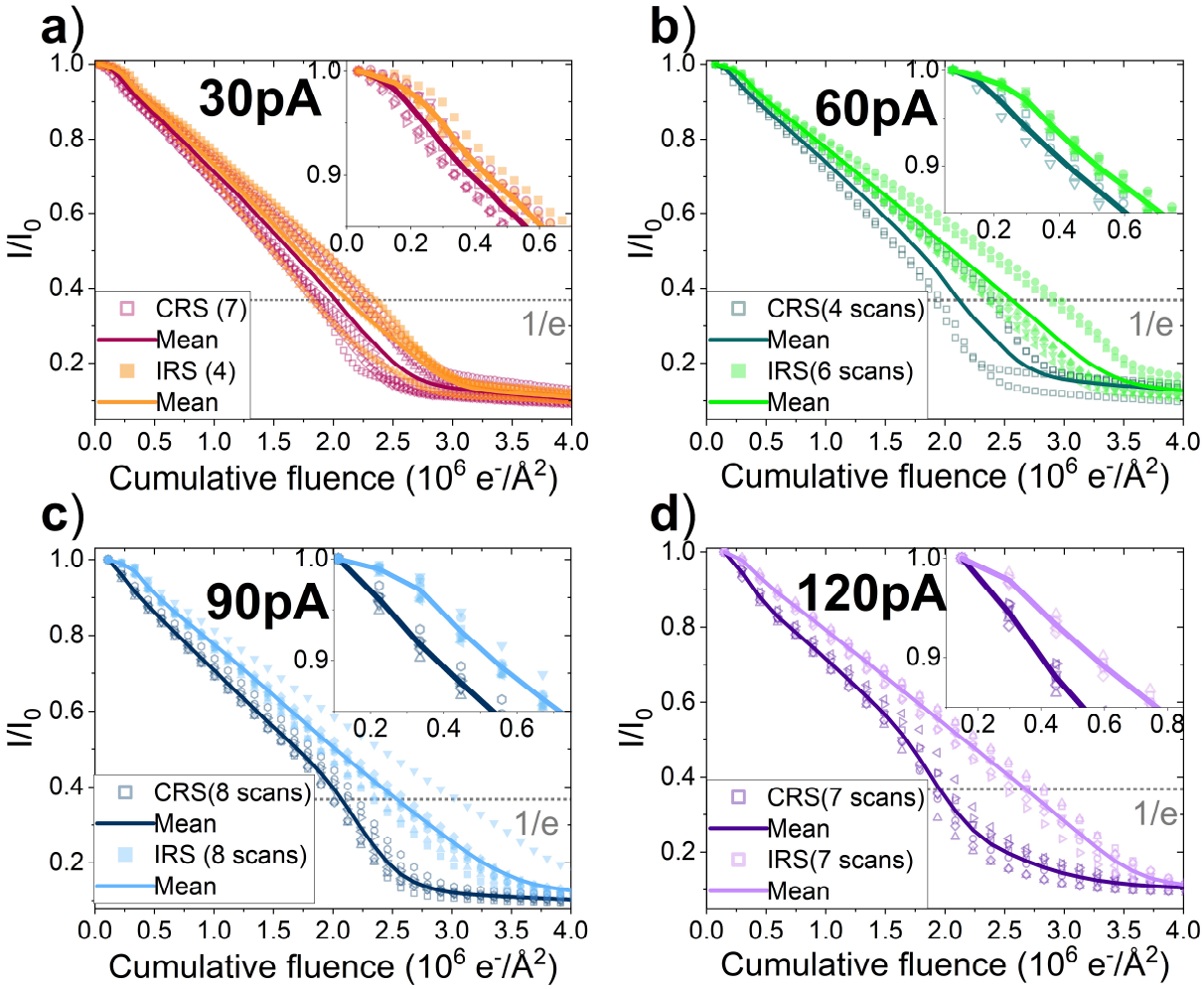

Figure 65. Mean frame HAADF intensity decay for conventional and interleaved raster scan are compared at different probe currents of a) 30 pA, b) 60 pA, c) 90 pA and d) 120 pA at a constant probe spacing of 1.6nm. Each curve is an average of 4 to 8 damage experiments.

The averaged values of C_F measured from the single acquisition data shown in Figure 65 are plotted in Figure 66a) and listed in Table 7. As shown in Figure 66a, imaging with CRS at different probe currents resulted in relatively similar C_F values ranging from 2.12 x 106 e-/Å2 to 2.29 x 106 e-/Å2. However here these C_F values underestimate the actual damage as the C_F values are determined from the linear fits and do not account for the accelerated intensity decay rates observed at higher cumulative fluences for CRS (see Figure 65b-d at around 2 106 e-/Å2). To account for this accelerated damage observed for CRS scans from 60-120pA, additional C_F values were estimated from the mean intensity decay plots

shown in Figure 65 and listed as additional values in brackets in Table 7. These C_F values decrease slightly with increasing beam current, consistent with the greater damage induced at higher electron flux. Compared to CRS, IRS results in overall larger C_F values, ranging from 2.25 x 10^6 $e^-/Å^2$ to 2.68 x 10^6 $e^-/Å^2$ indicating slower damage. Moreover, C_F for interleaved raster scan increases with higher probe currents, further indicating slower damage at higher flux. The efficiency for interleaved raster in mitigating damage improves with increasing electron flux from 5% at 30pA to 22% at 120pA. However, it has to be noted that the C_F values of CRS and IRS for 30 and 60pA are within their margin of error.

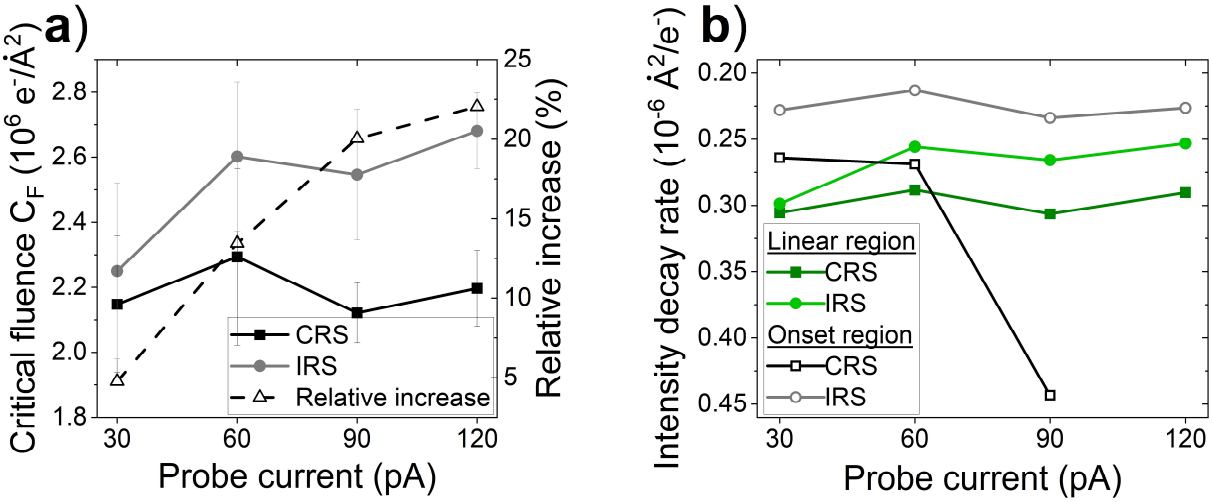

Figure 66. a) Critical Fluence C_F and b) intensity decay rates for onset and linear region for different probe currents and scan patterns: conventional (CRS) and interleaved raster scan (IRS); all measurements are for LiF on Si_xN_y with 1.6nm probe spacing; relative increase indicates the increase of C_F for interleaved compared to conventional raster scan.

In Figure 67 spatial distribution of C_F values is shown for a single exemplary experiment for each of the different probe flux and scan patterns. For IRS, independent of probe flux, spatial differences in damage are mostly dominated by preferred damage at grain boundaries. This is also valid for CRS at 30 and 60pA. For CRS at 120pA clear preferential damage at the bottom and the right side of the frame is shown. For CRS at 90pA, a similar effect is observed but to a lower extent. The change in mean frame intensity decay with increasing cumulative fluence observed for CRS at 120pA (see Figure 65d), are probably related to the large spatial differences in damage observed for CRS at 120pA shown in Figure 67.

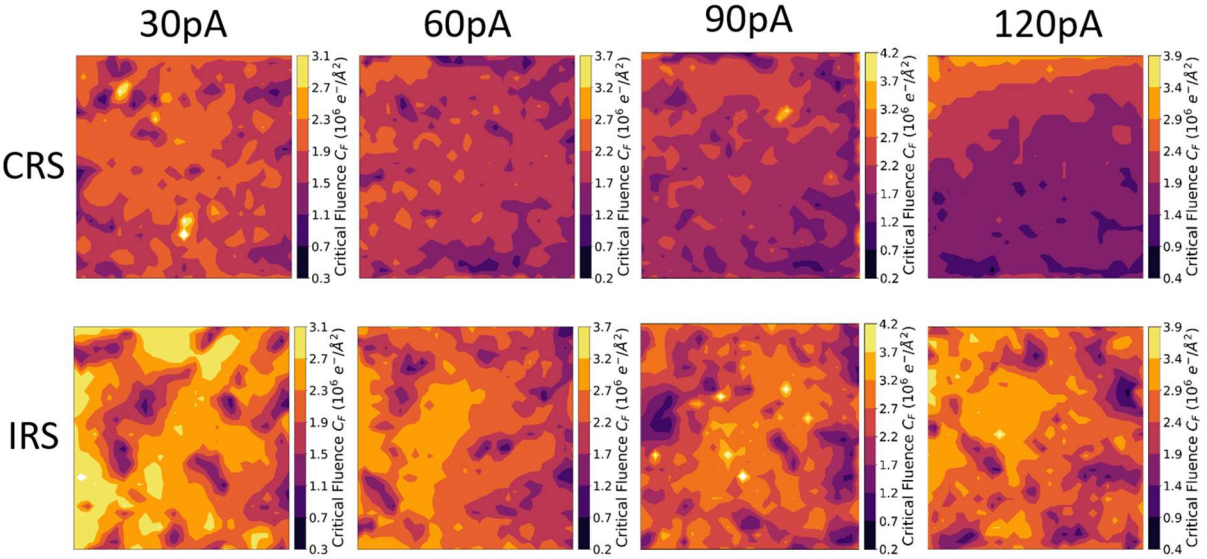

Figure 67. C_F maps for different scan patterns and probe fluence.

Table 7. Critical Fluence C_F at different probe currents I_b and scan patterns.

I_b	C_F 10^6 e$^-$/Å^2		
(pA)	**CRS**	**IRS**	**Rel. incr.**
30	2.15 ± 0.21	2.25±0.27	5%
60	2.29 ± 0.27 (2.1)	2.60±0.23	13%
90	2.12 ± 0.09 (2.07)	2.55±0.20	20%
120	2.20 ± 0.11 (1.95)	2.68±0.12	22%

CRS: conventional raster scan, IRS: interleaved raster scan, rel. incr.: relative increase of IRS compared to CRS. Additional C_F values for raster scan are given in brackets for plots with linear intensity decay accelerating at high fluence and were determined from mean values from the plot. All measurements are on LiF on Si_xN_y with 1.6nm probe spacing.

Table 8. DOD at different probe currents I_b and scan patterns.

I_b	I(DOD)			Φ_c(DOD) (10^6 e$^-$/Å^2)		
(pA)	**CRS**	**IRS**	**Δ**	**CRS**	**IRS**	**Rel. incr.**
30	0.058 ± 0.007	0.068 ± 0.004	0.010	0.255 ± 0.059	0.335 ± 0.030	31%
60	0.060 ± 0.011	0.071 ± 0.009	0.011	0.298 ± 0.061	0.410 ± 0.041	38%
90	0.056 ± 0.015	0.088± 0.014	0.033	0.237 ± 0.040	0.489 ± 0.058	106%
120	-	0.067 ± 0.007	-	-	0.447	-

CRS: conventional raster scan, IRS: interleaved raster scan, rel. incr.: relative increase of IRS compared to CRS; all measurements are on LiF on Si_xN_y with 1.6nm probe spacing.

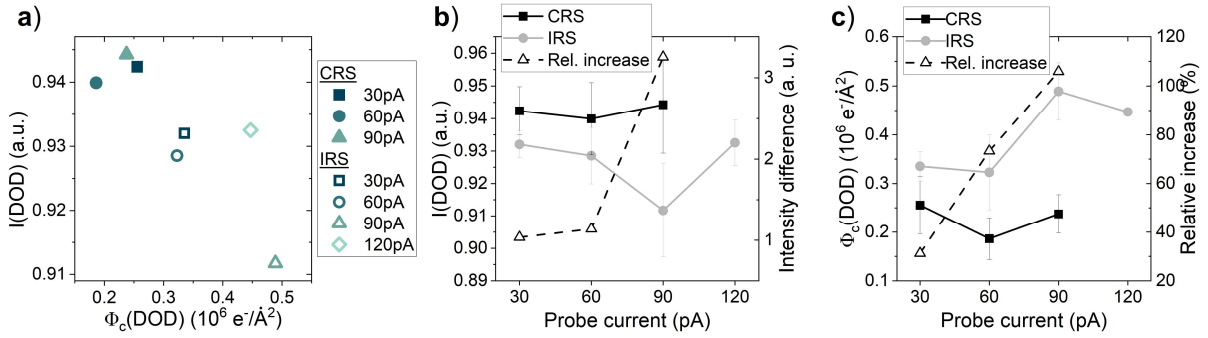

Figure 68. Comparing damage induced by conventional raster and interleaved raster scans for different probe flux with a) intensity and fluence values at the end of the onset decay, b) fluence onset decay and c) intensity loss by onset decay.

The averaged values of DOD measured from the single acquisition data shown in Figure 65 are plotted in Figure 68 and listed in Table 8. For CRS the DOD extend is similar for different probe currents, with intensity dropping by approximately 6% by a cumulative fluence of approximately 0.2 10^6 e$^-$/Å^2. For CRS at 120pA the graph is not following the classical intensity decay observed for the other acquisition conditions (see Figure 65d). Here, no DOD values could be determined. For IRS, DOD is overall larger compared to CRS for both the extend of intensity and cumulative fluence values. At 30 and 60pA the DOD extend is relatively similar and comparably lower to DOD values at 90 and 120pA.

In Figure 66b) and Table 9 the mean intensity decay rates for onset region, r_{onset}, and linear region, r_{linear}, are shown, which were determined from the graphs in Figure 65. For CRS, r_{linear} shows similar values over different probe currents. For IRS, r_{linear} is highest at 30pA compared to relatively similar lower values from 60 to 120pA. The difference between r_{linear} for CRS and IRS is negligible at 30pA, while at higher beam currents the difference is relatively similar with 11-13%.

For IRS, r_{onset} is relatively constant over different probe currents (0.21-0.23 x 10^{-6} Å^2/e$^-$) and consistently slower compared to its r_{linear}. As r_{linear} slightly decreases, the intensity decay rates for the two regimes become more similar with increasing flux. For IRS, the relative difference of r_{onset} compared to r_{linear} is

ranging from 31% slower decay in the onset at 30pA to 12% slower intensity decay in the onset region at 120pA (see relative difference IRS in Table 9).

For CRS, the r_{onset} increases with higher flux, from 0.26 x 10^{-6} Å^2/e$^-$ at 30pA to 0.44 x 10^{-6} Å^2/e$^-$ at 90pA. As at 120pA no DOD values could be determined for CRS, no r_{onset} could be determined here. Compared to the relatively constant r_{linear} values, r_{onset} values are slower at 30pA (16% slower) and 60pA (7% slower) and faster at 90pA (31% faster) for CRS (see relative difference CRS in Table 9).

Table 9. Intensity decay rates of linear regions and onset regions at different probe currents and scan patterns.

	Intensity decay rate						Relative difference onset vs. linear region	
I_b	r_{onset} (10^{-6} Å^2/e$^-$)			r_{linear} (10^{-6} Å^2/e$^-$)				
(pA)	**CRS**	**IRS**	**Rel. decr.**	**CRS**	**IRS**	**Rel. decr.**	**CRS**	**IRS**
30	0.264	0.228	13%	0.31	0.30	2%	+16%	+31%
60	0.269	0.213	21%	0.29	0.26	11%	+7%	+20%
90	0.443	0.234	47%	0.31	0.27	13%	-31%	+13%
120	-	0.23	-	0.29	0.25	13%	-	+12%

CRS: conventional raster scan, IRS: interleaved raster scan; rel. decr.: relative decrease of intensity decay rate of IRS compared to CRS ((IRS–CRS)/CRS); rel. diff. onset vs. linear region CRS or IRS relative difference of intensity decay rate in onset versus linear region ((onset–linear)/linear) for CRS and IRS respectively, indicating how much slower (rel. diff > 0) or faster (rel. diff < 0) onset region damage rates are compared to linear region damage rates; all experiments were acquired at 90pA and 1.6nm probe spacing for LiF on a silicon nitride substrate.

While DOD and therefore r_{onset} could not be determined at 120pA for CRS, investigating the shift of the main linear intensity decay from the starting point by the onset decay can still provide information about the relative r_{onset} compared to r_{linear}. In Figure 69 and Table 10, values for the linear region shift by the onset intensity decay ($\Delta I_{o\rightarrow I}$ and $\Delta\Phi_{o\rightarrow I}$) are shown, which were determined form the graphs in Figure 65. Positive and negative shift values indicate slower and faster intensity decay rates for the onset region compared to the linear region respectively. For IRS, all shift values are positive and decreasing with increasing probe flux, indicating overall slower intensity decay in onset compared to linear region. This is consistent with the comparison made above where r_{onset} was compared to r_{linear}. For CRS, relative shift values are decreasing with increasing probe flux, with positive values for 30 and 60pA and negative values for 90 and 120pA. Again, here the trend for 30 to 90pA is identical to the one observed above for comparing absolute intensity decay rates in onset and linear region. For 120pA, highest difference between intensity decay rate in onset and linear region are observed. As the intensity decay in the linear region is constant over different beam currents for CRS, the intensity decay in the onset region can be expected to be the highest among the different probe currents.

Table 10. Shift of the linear decay region by the onset region for different probe spacings and scan patterns

I_b (pA)	Cumulative fluence shift $\Delta\Phi_{o\to l}$ (10^6 e$^-$/Å^2)			Intensity decay shift $\Delta I_{o\to l}$		
	CRS	**IRS**	**Δ**	**CRS**	**IRS**	**Δ**
30	0.028	0.069	0.041	0.008	0.021	0.013
60	0.009	0.053	0.043	0.003	0.014	0.011
90	-0.056	0.043	0.099	-0.017	0.011	0.029
120	-0.135	0.032	0.167	-0.039	0.008	0.047

CRS: conventional raster scan, IRS: interleaved raster scan, Δ absolute difference between CRS and IRS values, negative and positive shift values indicate faster and slower intensity decay in onset region compared to linear region respectively

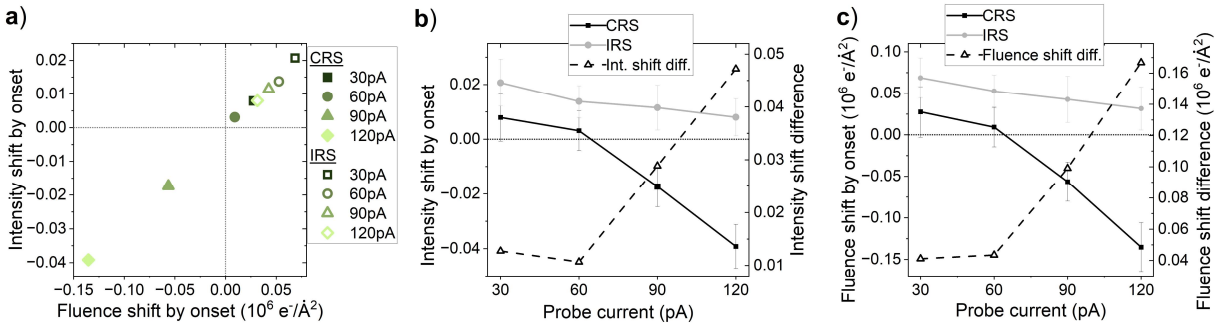

Figure 69. Onset decay compared relative to main linear decay rate intensity and fluence shift by onset decay relative to linear decay Comparing damage induced by for conventional raster and interleaved raster scans for different probe flux with a), b) relative fluence shift by onset decay relative to linear decay and c) relative intensity shift by onset decay relative to linear decay.

The applied electron flux can influence the resulting damage, specific to the imaged sample and flux range. Charging samples can show direct fluence rate effects (more damage with increasing flux), while diffusion limited mass loss has been associated with inverse fluence rate effects (slower damage at higher flux) [1]. Here, the insulating LiF sample could potentially show either, as it is prone to charging and shows diffusion limited mass loss.

CRS shows a direct dose rate effect as damage increases with the applied probe flux. The onset region is most heavily affected by increased probe flux. Interestingly, once the linear region is reached intensity decay rates are similar for different probe currents and radiation sensitivity of the material seems temporarily independent of probe flux. At increased cumulative fluence however, intensity decay rates suddenly increase. This effect is negligible for 30pA, small for 60pA and further increasing with probe current.

This indicates a competing damage mechanism that is influenced by both flux and cumulative fluence. The observation of damage dynamics changed for both parameters: high cumulative fluence and direct flux dependency have been reported in literature to indicate a charging related damage mechanism [1,16]. Above a certain threshold value, the electron beam can induce an electric field potential which reaches a steady state after a certain cumulative fluence. The higher the flux, the faster the steady state is reached and the larger is the generated electric field potential [16].

In contrast, IRS shows higher C_F with increasing flux, indicating slower damage and therefore an indirect flux dependency, suggesting a diffusion limited damage mechanisms [1]. For IRS, the intensity decay rate in the onset region is hardly affected by probe flux, contrary to CRS. In the linear region, intensity decay rates decrease with increasing flux and no accelerated damage regions are observed at higher cumulative fluences.

For another alkali halide sample (14nm thick NaCl on C substrate) an inverse dose rate effect has been reported [17], where charging effects are probably mitigated by the carbon substrate.

Comparing the flux influence for the two scan patterns, CRS shows a direct flux effect, while interleaved raster scan shows an inverse dose rate effect. This implies that the spatio temporal fluence distribution imposed by the scan pattern, can shift the damage dynamics. IRS preserves diffusion limited mass loss and circumvents charging effects, that accelerate damage in CRS.

5.1.3.4 Comparing CRS and IRS to other non-raster based interleaved scan patterns

Beside IRS, additional interleaved scan patterns were tested and compared to CRS, for the 90pA experiments on LiF on silicon nitride substrate with 1.6nm probe spacing. Unlike IRS these interleaved scan patterns do not have raster scan base but consist of sparse scans of snake and Hilbert patterns. Additionally, the subsequent subscans are rotated by 90 degrees. The scan patterns are a rotated interleaved snake scan (RISS) and a rotated interleaved Hilbert scan (RIHS). In Figure 70 normalized mean frame intensity decay are plotted for CRS (8 experiments), IRS (8 experiments), RISS (7 experiments) and RIHS (7 experiments) as scatter plots and each of their average as line plots.

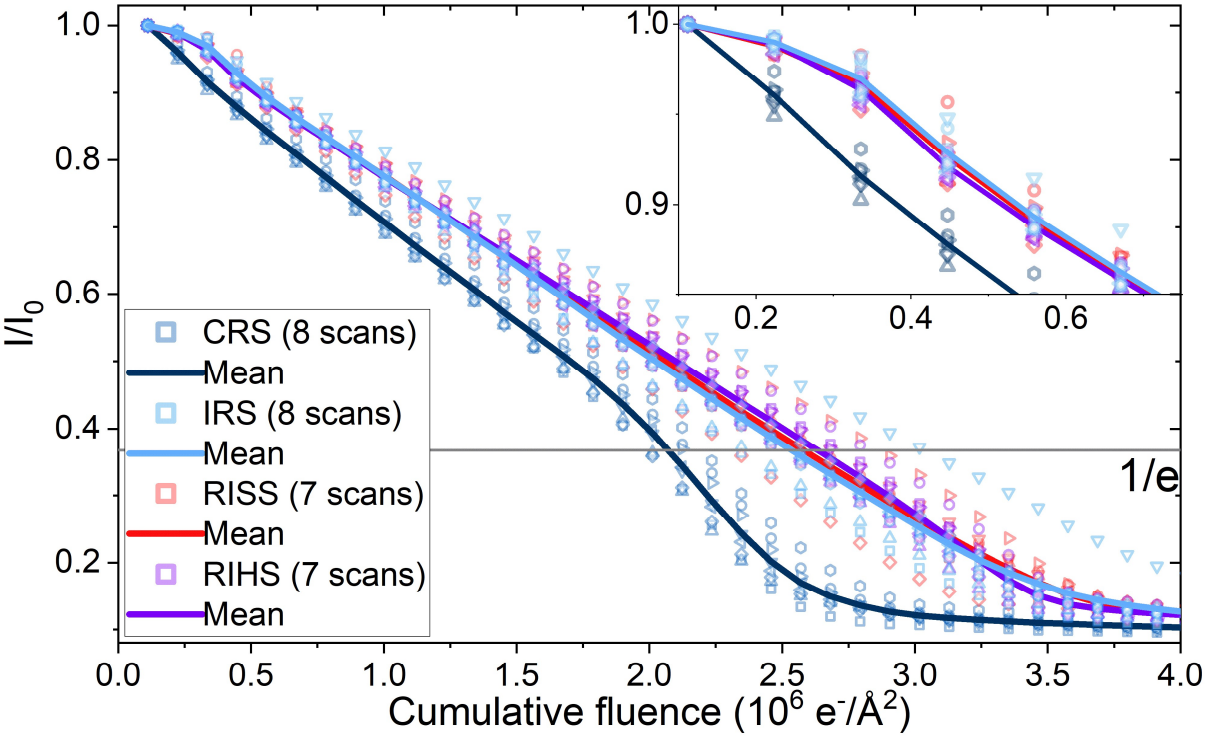

Figure 70. Mean frame HAADF intensity decay for different scan patterns at 90 pA and 1.6nm probe spacing. Each curve is an average of 7 to 8 damage experiments.CRS: conventional raster scan, IRS: interleaved raster scan, RISS: rotated interleaved raster scan, RIHS: rotated interleaved Hilbert scan.

The C_F-values for the different scan patterns were determined from the experiments displayed in Figure 70, and listed in Table 11. For RISS and RIHS; both, CF and DOD are similar to the values obtained for IRS and their values are within each other's error range. For CRS, C_F (2.12 x 10^6 $e^-/Å^2$) is lower compared to interleaved scan patterns where for IRS its C_F of 2.55 x 10^6 $e^-/Å^2$ is 20% higher, for RISS its C_F of 2.59 x 10^6 $e^-/Å^2$ is 22% higher and RIHS its C_F of 2.63 x 10^6 $e^-/Å^2$ is 24% higher.

In Figure 71 the C_F maps for the four different scan patterns are compared. As discussed before there is a spatio-temporal difference in the damage distribution between CRS and IRS. Here, for the two extra interleaved scan patterns, RISS and RIHS, damage distribution is similar to IRS, with spatial differences in damage that can be mostly attributed to increased damage at the grain boundaries.

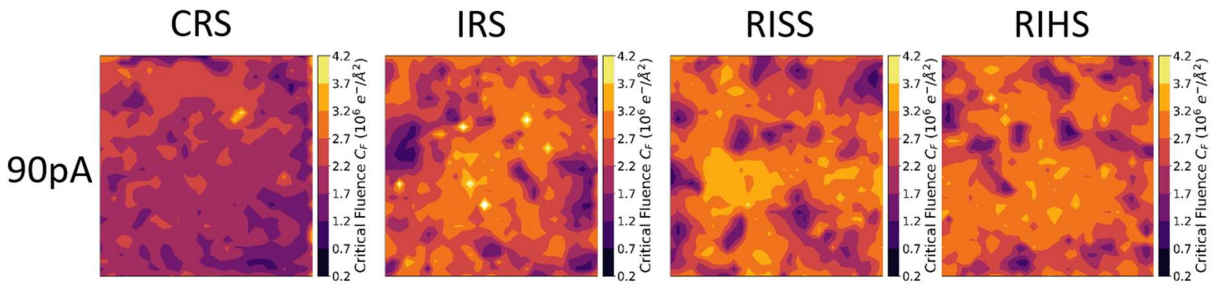

Figure 71. Spatial map of C_F for different scan patterns CRS: conventional raster scan, IRS: interleaved raster scan, RISS: rotated interleaved raster scan, RIHS rotated interleaved Hilbert scan; all measurements are at 90pA on LiF with silicon nitride substrate.

Table 11. CF and DOD values for different scan patterns.

Scan pattern	C_F 10^6 e$^-$/Å^2	Rel incr.	DOD I(DOD)	Δ	Φ_c(DOD) 10^6 e$^-$/Å^2	Rel. incr.
CRS	2.12±0.09		0.056±0.015		0.237±0.040	
IRS	2.55±0.20	20%	0.088±0.014	0.033	0.489±0.058	106%
RISS	2.59±0.17	22%	0.089±0.011	0.033	0.479±0.055	102%
RIHS	2.63±0.13	24%	0.090±0.013	0.034	0.463±0.042	95%

CRS: conventional raster scan, IRS: interleaved raster scan, RISS: rotated interleaved raster scan, RIHS: rotated interleaved Hilbert scan; rel. incr.: relative increase of interleaved scan compared to CRS; all experiments were acquired at 90pA and 1.6nm probe spacing for LiF on a silicon nitride substrate.

Table 12. Intensity decay rates for onset region and linear region for different scan patterns.

Scan pattern	Intensity decay rate r_{onset} (10^{-6} Å^2/e$^-$)	Rel. decr.	r_{linear} (10^{-6} Å^2/e$^-$)	Rel. decr.	Rel. diff. r_{onset} vs r_{linear}
CRS	0.443		0.306		+45%
IRS	0.234	47%	0.266	13%	-12%
RISS	0.242	45%	0.259	16%	-6%
RIHS	0.255	42%	0.251	18%	+2%

CRS: conventional raster scan, IRS: interleaved raster scan, RISS: rotated interleaved raster scan, RIHS: rotated interleaved Hilbert scan; rel. decr.: relative decrease of intensity decay rate of interleaved scan compared to CRS ((interl. Scan–CRS)/CRS); rel. diff. onset vs. linear region CRS or IRS relative difference of intensity decay rate in onset versus linear region ((onset–linear)/linear) for CRS and IRS respectively, indicating how much slower (rel. diff > 0) or faster (rel. diff < 0) onset region damage rates are compared to linear region damage rates; all experiments were acquired at 90pA and 1.6nm probe spacing for LiF on a silicon nitride substrate.

DOD for the different scan patterns were determined from the experiments displayed in Figure 70, and listed in Table 11. The extend of the cumulative fluence onset is smallest for CRS with 0.24 x 10^6 e$^-$/Å^2 compared to all three interleaved scan patterns where for IRS, with Φ_c(DOD) = 0.49 x 10^6 e$^-$/Å^2, the onset extend is 106% larger, for RISS with Φ_c(DOD) = 0.48 x 10^6 e$^-$/Å^2, the onset extend is 102% larger and Φ_c(DOD) = 0.46 x 10^6 e$^-$/Å^2, the onset extend is 95% larger, compared to CRS.

Intensity decay rates for onset, and linear region (r_{onset} and r_{linear}) for the different scan patterns were determined from the experiments displayed in Figure 70, and listed in Table 12. Compared to CRS, both r_{onset} and r_{linear} are slower for all three interleaved scan patterns. While r_{onset} is the slowest for IRS (47% slower) and slightly less slow for RISS (45% slower) and RIHS (42% slower) compared to CRS, the

trend among the interleaved scan patterns is inversed for r_{linear}, where intensity decay is slowest for RIHS (18%) and slightly less slow for RISS (16% slower) and IRS (13% slower) compared to CRS.

For CRS, r_{onset} is 31% faster compared to its linear region, for RIHS the intensity decay rate in both regions is comparable, and for the other two scan patterns r_{onset} is slower by 7% for RISS and by 14% for IRS compared to its linear region.

In the acquisition conditions we applied, most of the damage mitigation seems to result from the interleaved nature of the scan pattern and additional alternation of scan direction did not result in significant damage mitigation compared to interleaved raster scan. Only slight variations were observed between the interleaved scan patterns that are well within each other's errors. Nevertheless, they show a trend, where increasing direction alternation (RIHS>RISS>IRS) resulted in slightly faster intensity decay in the onset, while the opposite trend was observed in the linear region resulting in overall slightly lower damage with increasing direction alternation in the scan.

5.1.3.5 Increased insulating environment: LiF on silicon dioxide substrate

One of the reasons why *in situ* investigations of SEI dynamics is so challenging is that not only key SEI components like LiF are electronically insulating but also the surrounding materials, like the electrolyte and the TEM windows of the liquid cell set-up, are also electrically insulating and susceptible to charging under electron irradiation [18,19]. In order to systematically assess the influence of an insulating environment on damage behavior of different scan patterns, LiF deposited on a silicon dioxide substrate is investigated. SiO_2 is a more insulating material compared to silicon nitride and therefore it is possible to isolate the impact of substrate-induced charging in the observed damage dynamics. This difference in insulating properties can be estimated in a simplified manner by their bandgaps, with a smaller band gap for Si_3N_4 of ~5.1eV [20] compared to the larger band gap for SiO_2 of ~8.9eV [20,21]. Damage experiments are conducted on LiF deposited on a silicon dioxide membrane in specific acquisition conditions identical to previous experiments on silicon nitride (60pA and 90pA at 1.6nm probe spacing). First damage experiments for LiF on silicon dioxide are compared for conventional raster, interleaved raster and rotated interleaved snake scan at 60pA and 90pA and compared to previous results on the silicon nitride membrane. Then spatio-temporal damage evolution is investigated and compared for the different scan patterns.

Damage experiments on LiF on SiO_2 substrate were conducted using conventional, interleaved raster, and rotated interleaved snake scan at probe fluxes of 60pA and 90pA (see Figure 72). Interleaved scan patterns show similar overall intensity decay as observed in previous section for experiments with silicon nitride substrates, while for CRS on SiO_2-substrate damage kinetics change to a non-linear decay after the damage onset, which can be correlated to spatial non-uniform damage distribution. Due to the change in damage dynamics, for CRS, C_F cannot be determined from the linear decay anymore. Instead, here it will be estimated from the mean plot and is listed in brackets in Table 13.

In Figure 72, for both 60pA and 90pA, interleaved raster exhibited extended onset decays and slower damage rates for lower cumulative fluence compared to conventional raster scan. At 60pA, rotated interleaved snake scan showed damage trends intermediate between conventional and interleaved raster scans (see Figure 72a)), whereas for LiF on silicon nitride, interleaved raster and rotated interleaved snake scan intensity decays were nearly identical (see Figure 65a)). Comparing the two probe fluxes, slower damage is observed for higher flux, with this trend being less pronounced for conventional raster scans and more apparent for interleaved raster scan (see Figure 70)). Overall, LiF on SiO_2 exhibited extended damage onset decays and increased damage rates compared to Si_3N_4 (see Figure 73). Despite these differences, the general trends, such as slowed damage for interleaved scanning and the increased efficiency of interleaved scans in mitigating damage at higher flux, remained consistent between the two substrates.

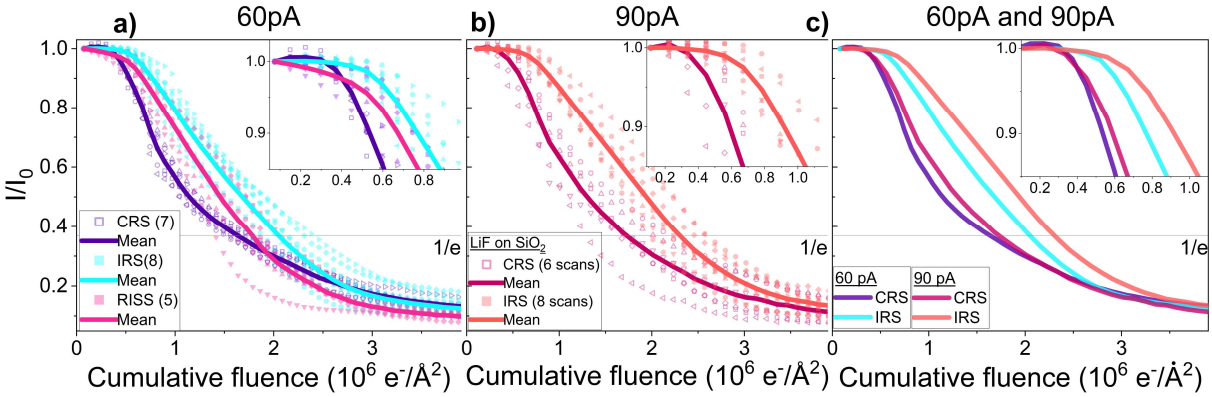

Figure 72 Comparing damage for raster, interleaved raster and rotated interleaved snake scan on LiF on silicon dioxide substrate at 1.6 nm probe spacing with a) 60 pA probe current and b) 90 pA probe current and c) comparing mean intensity decays for 60 pA and 90 pA.

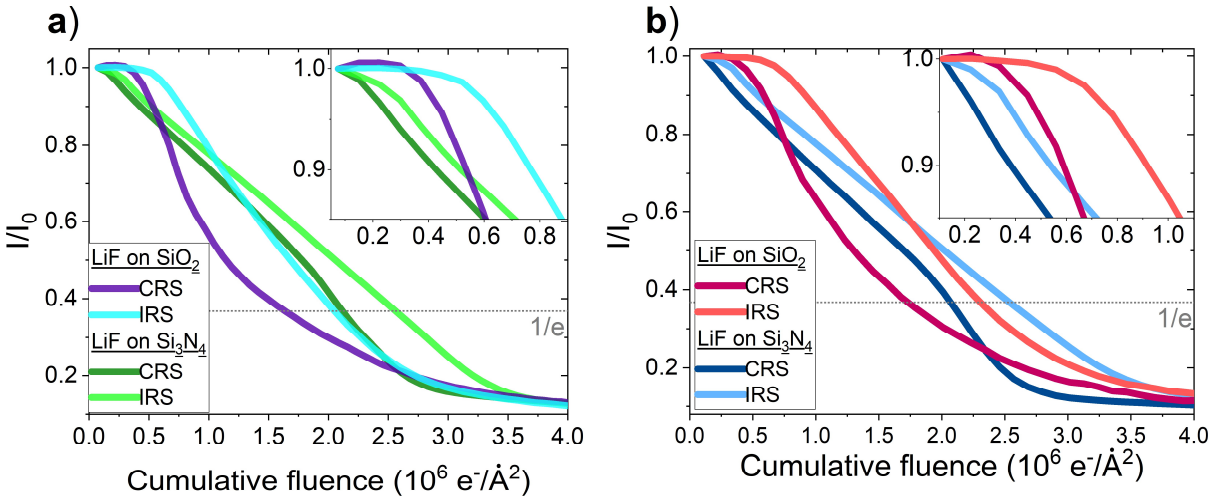

Figure 73. Comparing mean damage decay for LiF on silicon nitride and silicon oxide for 60 and 90pA for conventional and interleaved raster scan with 1.6 nm probe spacing.

In Table 13 mean C_F values are listed, which were determined from the plots in Figure 72. The mean C_F values for CRS were determined from the mean line plots. For IRS and RISS mean C_F values are determined by an average from the C_F values determined from single scatter plots. CRS has smaller C_F values compared to interleaved scan patterns, independent of the probe current, with 34% larger C_F for IRS at 90pA and 25% larger C_F for IRS at 60pA. For RISS at 60pA C_F is in between IRS and CRS.

In Table 14 mean DOD values are listed for IRS and RISS at 60 and 90pA which were determined from the plots in Figure 72. DOD values for CRS could not be determined due to the change in damage dynamics for the mean frame intensity decay. The extend of Φ_c(DOD) is larger for IRS compared to RISS and larger for IRS at 90pA compared to IRS at 60pA.

In Table 15 intensity decay rates for onset and linear region are listed for IRS and RISS at 60 and 90pA, which were determined from the plots in Figure 72. For CRS Intensity decay rates could not be determined due to the change in damage dynamics for the mean frame intensity decay. Intensity decay rates in the both regions follow the trend for C_F values with lower intensity decay rates at 90pA for IRS, compared to the interleaved scans at 60pA, where IRS was decaying slower compared to RISS. For both IRS and RISS, the onset region exhibits an approximately 70% slower intensity decay rate compared to the linear region.

Table 13. C_F spacing for LiF on SiO_2 substrate *for different probe currents and scan patterns.*

I_b			C_F 10^6 $e^-/Å^2$		
(pA)	**CRS**	**IRS**	**Rel. incr.**	**RISS**	**Rel. incr.**
60	(1.64)	1.96 ± 0.18 (2.05)	25%	1.74 ± 0.27 (1.79)	9%
90	(1.73)	2.29 ± 0.23 (2.31)	34%	-	-

Values in brackets for C_F estimated from mean line plot in graphs opposed to C_F estimation from linear slope. CRS: conventional raster scan, IRS: interleaved raster scan, RISS: rotated interleaved raster scan; rel. incr.: relative increase of interleaved scan compared to CRS; all experiments were acquired at 1.6nm probe spacing.

Table 14. DOD for LiF on SiO_2 substrate for different scan patterns and probe currents.

I_b	I(DOD)			Φ_e(DOD) (10^6 $e^-/Å^2$)		
(pA)	**IRS**	**RISS**	**Δ**	**IRS**	**RISS**	**Rel. decr.**
60	0.90±0.06	0.91±0.02	0.01	0.75±0.13	0.66±0.06	13%
90	0.91±0.03			0.91±0.14		

CRS: conventional raster scan, IRS: interleaved raster scan, RISS: rotated interleaved raster scan; rel. incr.: relative increase of interleaved scan compared to CRS; all experiments were acquired at 1.6nm probe spacing.

Table 15. Intensity decay rates of onset regions and linear regions for LiF on SiO_2 substrate at different probe currents and scan patterns.

I_b	Intensity decay rate Onset region (10^{-6} $Å^2/e^-$)			Linear region (10^{-6} $Å^2/e^-$)			Relative difference onset versus linear region	
(pA)	**IRS**	**RISS**	**Rel. diff.**	**IRS**	**RISS**	**Rel. decr.**	**IRS**	**RISS**
60	0.147	0.149	2%	0.446	0.516	15%	67%	71%
90	0.113	-		0.396		-	71%	--

CRS: conventional raster scan, IRS: interleaved raster scan; RISS: rotated interleaved raster scan,rel. decr.: relative decrease of intensity decay rate of RISS compared to IRS ((RISS–IRS)/IRS); rel. diff. onset vs. linear region IRS or RISS relative difference of intensity decay rate in onset versus linear region ((onset–linear)/linear) for IRS and RISS respectively, indicating how much slower (rel. diff > 0) or faster (rel. diff < 0) onset region damage rates are compared to linear region damage rates; all experiments were acquired at 90pA and 1.6nm probe spacing for LiF on a silicon nitride substrate.

In Figure 74 and Figure 75 contour maps with the spatial distribution of C_F are shown for probe currents of 60pA and 90pA respectively for LiF experiments on SiO_2 substrate for different scan patterns.

For CRS, damage is spatially non-uniform: at lower cumulative fluences, C_F is first reached in the lower right corner of the scanned area, progressing upward. The C_F values in the lower part of the frame are the lowest, while the C_F values in the upper most part in the frame show the highest intensities compared to IRS and RISS experiments. This trend is very reproducible for the CRS experiments at 60pA (Figure 74) and moderately reproducible for the CRS experiments at 90pA (see Figure 75). For the latter still, overall smallest C_F values are found compared to other scan patterns, but in few cases the high C_F values observed in the upper part of the frame are negligibly low. In comparison, IRS damage is more spatially uniform, with lowest C_F on the right-hand side of the field of view and increasing to the left. For IRS no trend along the slow scan direction is observed. This trend is highly reproducible for the 90pA measurements (see IRS in Figure 75). For IRS at 60pA (see Figure 74), accelerated damage on the right side can be observed in most C_F similar to IRS at 90pA, with a few exemptions where the trend is less pronounced. The RISS at 60pA (see Figure 74) exhibit the most spatially uniform C_F value distribution. In all three scan patterns, slower mass loss is observed at the outer edges of the frame.

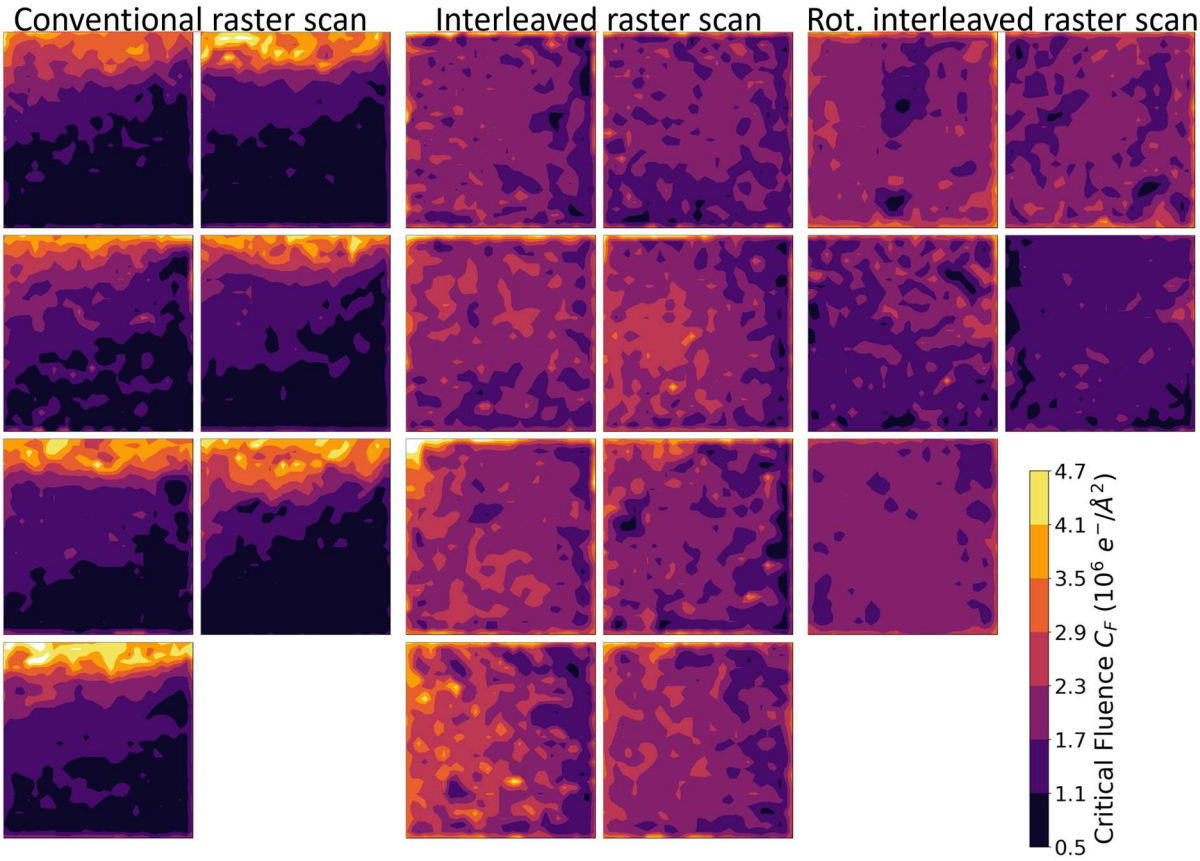

Figure 74. C_F maps for experiments on LiF on SiO_2 substrate at 60pA for different scan patterns.

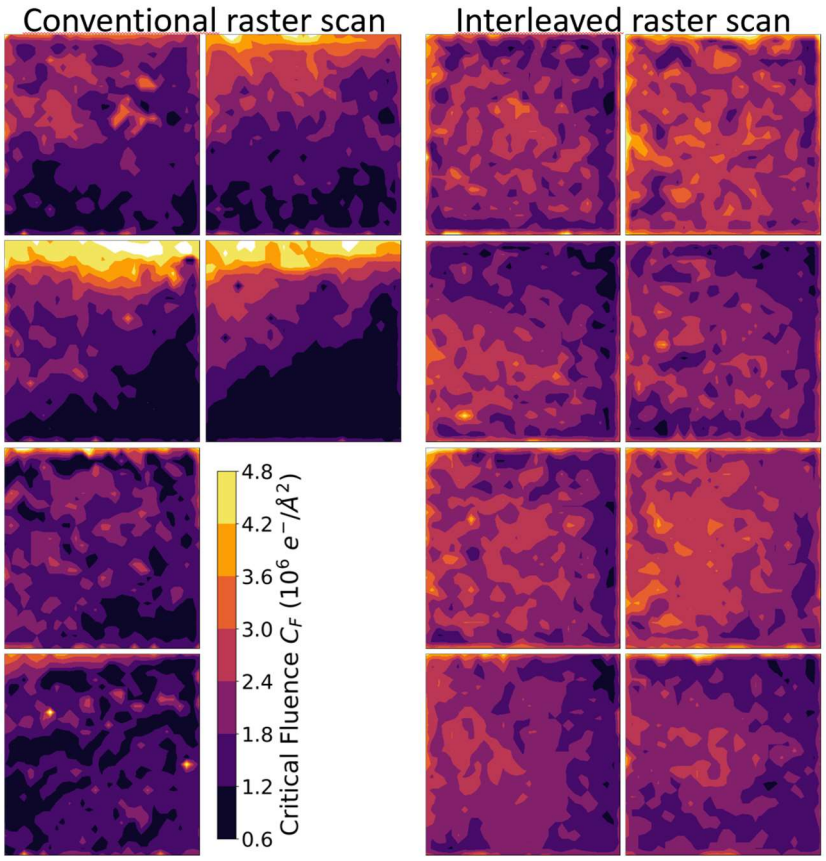

Figure 75. C_F maps for experiments on LiF on SiO_2 substrate at 90pA for different scan patterns.

For IRS and RISS the mean frame intensity decay (see Figure 72) still roughly describes the intensity decay in each part of the frame, as can be seen by the small differences of C_F values in the C_F maps above (see IRS and RISS in Figure 74 and Figure 75). For CRS on the other hand mean frame intensity decay (see Figure 72) does not represent the strong local differences over the frame, as can be seen by the large contrast differences in the C_F maps above (see CRS in Figure 74 and Figure 75). Consequently, C_F determined from the mean frame intensity decay here holds a different meaning for CRS compared to IRS and RISS.

In contrast to the spatially non-uniform damage decay observed on silicon dioxide, LiF on silicon nitride exhibits comparably uniform spatio-temporal damage distribution in most acquisition conditions as can be seen in Figure 59, Figure 67 and Figure 71. However, for acquisition conditions promoting charging, such as elevated beam currents and low probe spacing, also spatially non-uniform damage for CRS on silicon nitride can be observed, as can be seen in Figure 67 for CRS at 90pA and 120pA at 1.6nm probe spacing. At 90pA CRS shows slightly preferential damage in the lower right corner at higher cumulative fluences, while at 120pA CRS shows clear spatial inhomogeneous damage trends that are also resulting in differences in the mean intensity decay, resembling those observed for LiF on silicon dioxide.

In Figure 76, horizontal and vertical line plots are shown for three different scan patterns from the 60pA experiments for LiF on SiO_2 (see Figure 74), to further investigate spatial difference in damage over the whole cumulative fluence range. Due to low signal to noise ratio, line scans were binned over 8x128 pixels, resulting in 16 binned line scans over the frame area (see schematic display of bins in Figure 76). Comparing vertical and horizontal line scans give insights on intensity decay differences from left to right and top to bottom of the frame area respectively.

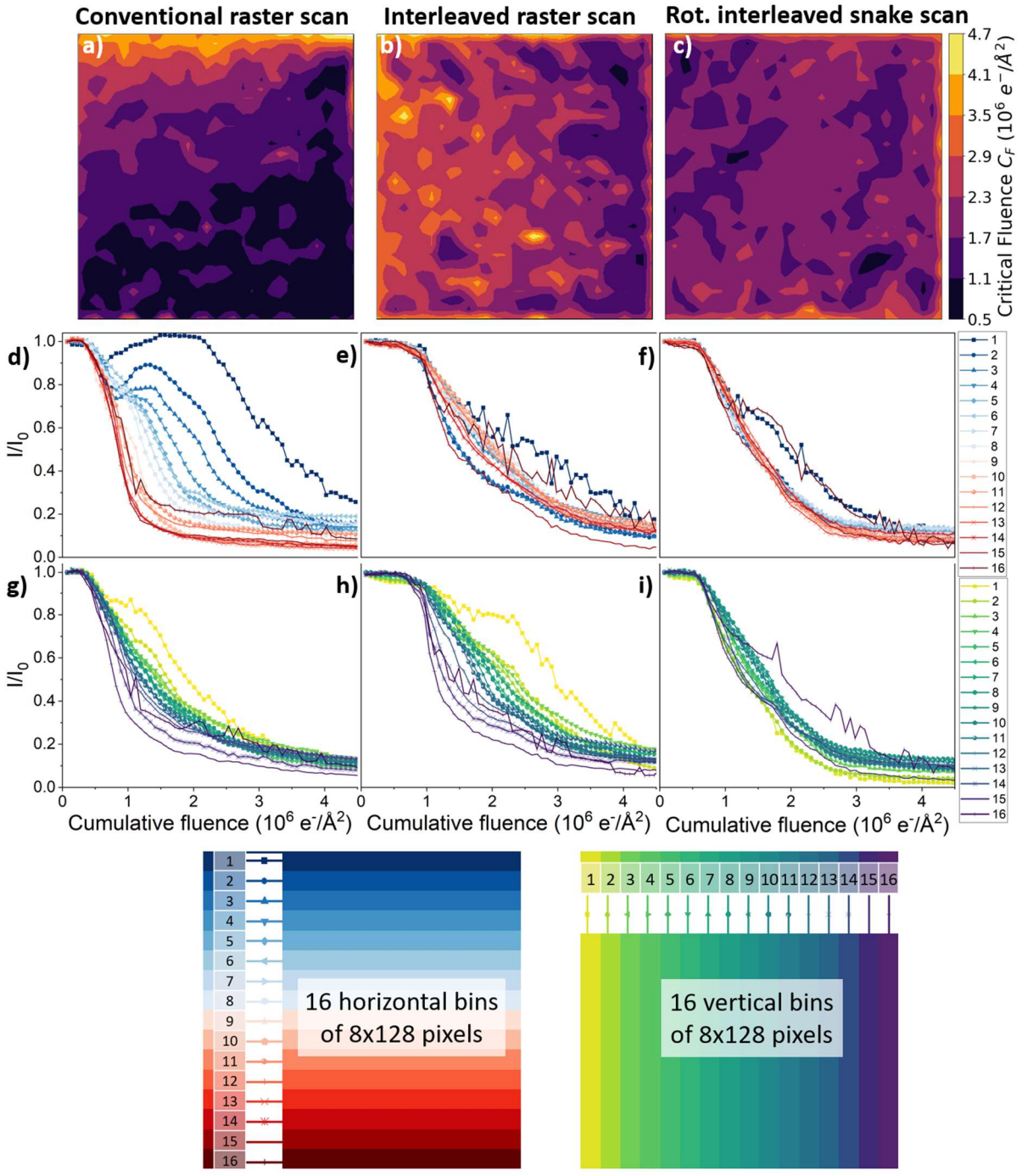

Figure 76. Spatial maps of critical fluence C_F for a) conventional raster scan, b) interleaved raster scan and c) rotated interleaved snake scan; intensity evolution with increasing cumulative fluence corresponding to plots in a)-c) for d)-f) horizontal and g)-f) vertical line plots as indicated in schematic bin overviews with 16 bins of each 8 x 128 pixels.

In Figure 76d) damage trends for CRS are compared from top to bottom with horizontal line plots. Intensity decay in the lower part of the scan decays similarly to the mean intensity decay of the frame. However, in the frame areas above, damage decay is slowed and in the uppermost line after an initial onset plateau and subsequent mass loss, intensity increases again (see plots 1-4 in Figure 76d)). When comparing damage trends over the frame from left to right for CRS (see Figure 76)g), mass loss is fastest on the right side and slows towards the left, a trend that is also observed for interleaved raster scan (see Figure 76h)). When comparing damage from top to bottom for IRS (see Figure 76e)), no areas with increasing intensity are observed contrary to the trend for CRS. The rotated interleaved snake scan shows the most uniform mass loss behavior for both comparisons from top to bottom (see Figure 76f))

and from left to right (see Figure 76i)). Here slowed mass loss is observed only in the outermost binned regions (see plots 1 and 16 in Figure 76f) and 16 in Figure 76i)), next to a region of accelerated mass loss, compared to adjacent areas. This effect is also observed for CRS and IRS (see plots 1 and 16 in Figure 76d), e), g), h)).

In another radiolysis damage study [7], highest damage is reported mainly in the center of the imaged area, for both raster and an interleaved scan patterns. This local damage hotspot has been correlated to largest overlap for mobile damage species accelerating damage in the center of the frame and has been supported by diffusion based simulations [6,8]. In our experiments however, the damage distribution depends on the scan pattern with a connection to fast and or slow scan direction and shows local damage effects at the border of the frame. A contributing factor for the observed differences in spatial damage distribution could be introduced by differences in fluence distribution by variation in probe current, more extreme probe spacing and dwell time and different sample and sample structure with grain boundaries. However, as this spatial effect appears mostly in conditions prone to favor charging the sample (silicon dioxide substrate, small probe spacing, large probe currents), it can be assumed that charging effects are contributing to the observed damage distribution.

In insulating systems, electron beam irradiation induces electron-deficient regions beneath the probe due to radiation induced secondary electron and Auger electron emission [1,18,22]. Above a certain electron flux threshold, the electron beam can induce an electric field potential, which is pointing perpendicular and outwards the electron probe for STEM experiments [16]. The generated electric field potential gradient can drive ion transport over nanometer-scale distances from the probe [16], with the most intense fields and charging effects localized at the probe periphery [23]. Expanding these local probe observations to a full frame acquisition, spatial differences in charging effects can be expected, as indicated by SEM studies. In SEM electron beam lithography experiments it has been shown that the raster probe motion can induce an electric field gradient over the imaged frame, that differs from the charge distribution induced by a snake or a spiral motion [24]. Both, random and interleaved scans have shown to reduce charging effects in STEM and SEM experiments [25,26].

A potential step at the frame border introduced by the potential difference of irradiated to non-irradiated, could explain the specific mass loss observed at the outer edges of the scanned frame observed for all three scan patterns, where the potential step could direct diffusion of charged defects species.

The spatial non-uniformity in conventional raster scan may be attributed to an electric field gradient induced by the raster scan pattern. This could explain the increase of intensity in the upper frame area in combination with accelerated mass loss in the lower frame area (see Figure 76a)) as a potential driven mass transport resulting in the progression of damage from the lower-right corner upward. In contrast, IRS resulted in a more homogeneous damage distribution along the slow scan direction, while damage along the fast scan axis remains similar to CRS with faster damage on the right-hand side. Increased sparsity of sub-scans by IRS helps to decorrelate interaction from one row to the next, but not from subsequently placed pixels within a scanned line, indicating a temporal damage factor. IRS seems to disrupt the potential gradient along the slow scan axis through delayed visitation of neighboring pixels, while it fails to do so along the fast scan axis. Additional directional alternation of scan direction, further cancels directional charging effects imposed by probe motion and leads to even more uniform damage distributions for rotated interleaved snake scanning. Alternation of the scan direction after each scanned row, seems to cancel the damage directionality within the scanned row observed for IRS. However, this direction alternation leads to spatio-temporal closer proximity of scan points in subsequently scanned rows leading to overall slightly accelerated damage compared to IRS.

In our work, the change to non-linear intensity decay for conventional raster scan at conditions susceptible to charging (more insulating SiO_2-substrate and increased flux for silicon nitride substrate) support the hypothesis that charging significantly influences damage kinetics, and that these effects can be mitigated by interleaved scanning. The extended onset observed for experiments on silicon oxide compared to silicon nitride could be due to the electric field induced perpendicular to the probe directing diffusion of charged damage species. For example, the mobile H-centers, consisting of a F_2^- molecule sharing a hole in a fluorine interstitial, should be affected by an electric field gradient. While mass loss can occur by H-center hopping to the surface, a horizontal electric field gradient probably induces directionality to the mobile fluorine species that is opposing the direct vertical direction to the sample surface, thereby delaying mass loss. Subsequent accelerated mass loss is likely a result of the electric field accelerating overall diffusion and stabilizing defects, by hindering recombination by spatially separating F- and H-centers through electric field-accelerated diffusion. The ability of interleaved scan patterns to mitigate damage suggests that these scan patterns allow relaxation of induced potential gradients by delaying the visitation of nearest neighbor positions. Charging effects occur above a certain threshold that is reached earlier with higher probe currents [16]. In a simulations supported SEM study it was shown that in a line scan previous line points can influence induced charging in subsequent scan points in a self-regulatory way, so that the field induced in the first scan points reduces secondary electron emission in subsequent scan points by their generated electric field [27]. Interleaved scans could distribute the induced fluence temporarily over a larger area, effectively reducing the induced charge density temporarily and potentially delaying the threshold charging values. Additionally, IRS spreading the fluence earlier over the full frame might regulate charging induced by subsequent subframes regulating charge induced effects earlier on compared to CRS.

5.1.3.6 Optimized acquisition conditions for low-damage imaging of LiF thin films

From the experiments in the sections above some general trends for optimized acquisition conditions can be summarized for imaging the polycrystalline LiF thin film sample.

Increased probe spacing mitigate damage more drastically than using alternative scans. But even at the highest probe spacing investigated here of 6.4 nm interleaved scanning still effectively mitigates beam damage compared to raster scanning.

Conventional raster scanning should be avoided at increased flux as here charging related damage phenomena are observed and a direct dose rate effect was found. Interleaved scans on the other hand showed an inverse dose rate behavior, enabling imaging at increased flux and therefore can help effectively to achieve acceptable SNR in damage sensitive samples.

For some acquisition conditions the onset region shows long plateaus where close to no mass loss can be detected. Imaging within this plateau region provides ideal conditions for close to damage free multi frame acquisition. Extended plateaus were observed for increased probe spacing, for interleaved scans opposed to raster scans and for LiF on the more insulating SiO_2 substrate, compared to the silicon nitride substrate. For LiF on the silicon dioxide substrate largely extended onset plateaus are observed, where even after 5 frames and a cumulative fluence of 0.56×10^6 $e^-/Å^2$ the intensity only decreased to 99% of its initial intensity. In comparison the same intensity drop is reached at the second frame at a cumulative fluence of 0.22×10^6 $e^-/Å^2$ for LiF on a silicon nitride substrate. However, it has to be noted that imaging on the more insulating silicon dioxide made the use of a drift correction necessary.

Imaging at interfaces should be avoided as much as possible as here damage is locally accelerated. For the example given in Figure 60 in section 5.1.3.1, the C_F at grain boundaries can be roughly estimated to be three to four times earlier compared to the mean frame C_F. In the next chapter damage will be

explored for monocrystalline LiF FIB-lamellas, enabling a direct comparison of the polycrystalline LiF sample used in this chapter to damage on a grain boundary free LiF sample.

Imaged information at all four outer frame borders should be handled with care as here local damage was observed independent of the applied scan. To avoid damage hot spots, especially in charging promoting conditions, imaging with interleaved scans is preferential compared to raster scan.

5.1.4 Conclusion and outlook

The influence of spatio-temporal fluence distribution on radiation damage in LiF was systematically investigated by varying scan pattern, probe spacing, and probe flux. Additionally, the role of having a substrate with higher or lower electrical resistivity is assessed by comparing LiF deposited on silicon nitride and the better electrical insulator silicon dioxide. Different interleaved scan patterns, based on raster scan and in some cases based on snake and Hilbert scan, were applied, to achieve more homogeneous fluence distribution within the constraints of our scan engine. The interleaved scan patterns were applied to the beam sensitive battery material LiF. The scans were executed by jumping from pixel to pixel similar to EELS spectrum image acquisition, which allowed to investigate the effect of probe spacing in both slow and fast scan directions. Interleaved raster scan was compared with conventional raster scan at different probe spacings, probe flux and substrates. Interleaved raster scan consistently resulted in less damage compared to conventional raster scans, with damage onsets extended up to double the cumulative fluence and critical fluences increased up to 22%. Efficiency of interleaved raster scan to mitigate damage is highest at smallest probe spacing and largest probe flux. Slower damage was observed with increased probe spacing in HAADF experiments, which could be correlated to slowed agglomeration of defects by low-loss EELS investigations. Furthermore, it was demonstrated that probe flux effects are scan-pattern-dependent, with higher flux decreasing damage for interleaved scans but increasing it for conventional raster scans. Lastly, the influence of substrate conductivity was investigated, where additionally rotated interleaved snake scan was compared beside the interleaved raster scan to raster scan. Replacing silicon nitride with the more insulating silicon dioxide substrate induced damage hotspots and mass transport for conventional raster scan, which interleaved raster scan mitigated in the slow scan direction, with rotated interleaved snake scan further reducing these effects in the fast scan direction. Additionally, largest onset plateaus with only minimum mass loss are observed for LiF on silicon dioxide, opening the opportunity for damage free investigation with limited frame number. While here the focus was on LiF, alternative scan patterns should be able to improve investigations in other radiolysis and charging prone samples, especially in *in situ* and operando studies where often insulating environments (e.g. liquid cell window membranes or insulating liquid) can't be circumvented and low dose conditions are not possible due to SNR limitations in spectroscopy applications. Integrating charging effects into damage-mitigation models would also enhance their predictive accuracy and provide deeper insights into the mechanisms at play. The presence of charge-induced effects in insulating samples present an opportunity for targeted experiments, such as STEM off-axis holography or 4D-STEM, to directly assess spatial charging dynamics. Also, incorporating charging effects into existing damage simulation models could refine their predictions to find low damage conditions.

In this chapter damage induced mass loss was investigated with HAADF experiments. In the next chapter complimentary monochromated STEM-EELS experiments on monocrystalline LiF thin films will be shown, extending insights of defect evolution and the role of interleaved scanning in damage mitigation from a spectroscopic view point.

Appendices

Appendix A Data analysis of

Appendix B Supplementary Information

Bibliography

[1] Lodico JJ, Mecklenburg M, Chan HL, Chen Y, Ling XY, Regan BC. Operando spectral imaging of the lithium ion battery's solid-electrolyte interphase. Science Advances 2023;9:eadg5135. https://doi.org/10.1126/sciadv.adg5135.
[2] Fultz B, Howe JM, editors. Diffraction Contrast in TEM Images. Transmission Electron Microscopy and Diffractometry of Materials, Berlin, Heidelberg: Springer; 2008, p. 337–421. https://doi.org/10.1007/978-3-540-73886-2_7.
[3] Chen Q, Dwyer C, Sheng G, Zhu C, Li X, Zheng C, et al. Imaging Beam-Sensitive Materials by Electron Microscopy. Advanced Materials 2020;32:1907619. https://doi.org/10.1002/adma.201907619.
[4] What is EELS? EELSInfo 2015. https://eels.info/about/overview (accessed July 5, 2026).
[5] Carter CB, Williams DB. Transmission Electron Microscopy: Diffraction, Imaging, and Spectrometry. Springer; 2016.
[6] Hobbs LW. Transmission Electron Microscopy of Extended Defects in Alkali Halide Crystals n.d.
[7] Hobbs LW. Radiation damage in electron microscopy of inorganic solids. Ultramicroscopy 1978;3:381–6. https://doi.org/10.1016/S0304-3991(78)80058-8.
[8] Radiation Effects in Analysis of Inorganic Specimens by TEM. Introduction to Analytical Electron Microscopy, Boston, MA: Springer US; 1979, p. 437–80. https://doi.org/10.1007/978-1-4757-5581-7_17.
[9] Egerton RF, Lazar S, Libera M. Delocalized radiation damage in polymers. Micron 2012;43:2–7. https://doi.org/10.1016/j.micron.2011.05.007.
[10] Egerton RF. Scattering delocalization and radiation damage in STEM-EELS. Ultramicroscopy 2017;180:115–24. https://doi.org/10.1016/j.ultramic.2017.02.007.
[11] McGilvery CM, Abellan P, Kłosowski MM, Livingston AG, Cabral JT, Ramasse QM, et al. Nanoscale Chemical Heterogeneity in Aromatic Polyamide Membranes for Reverse Osmosis Applications. ACS Appl Mater Interfaces 2020;12:19890–902. https://doi.org/10.1021/acsami.0c01473.
[12] Abellan P, Gautron E, LaVerne JA. Radiolysis of Thin Water Ice in Electron Microscopy. J Phys Chem C 2023;127:15336–45. https://doi.org/10.1021/acs.jpcc.3c02936.
[13] Egerton RF, Lazar S, Libera M. Delocalized radiation damage in polymers. Micron 2012;43:2–7. https://doi.org/10.1016/j.micron.2011.05.007.
[14] Arat KT, Klimpel T, Hagen CW. Model improvements to simulate charging in scanning electron microscope. J Micro/Nanolith MEMS MOEMS 2019;18:1. https://doi.org/10.1117/1.JMM.18.4.044003.
[15] Larsen MS, Hansen O, Zaluzec NJ, Mølhave KS, Yesibolati MN. Charges on a suspended silicon nitride membrane under a high-energy electron beam. Nanoscale 2025:10.1039.D5NR01742D. https://doi.org/10.1039/D5NR01742D.
[16] Jiang N. Note on in situ (scanning) transmission electron microscopy study of liquid samples. Ultramicroscopy 2017;179:81–3. https://doi.org/10.1016/j.ultramic.2017.04.012.
[17] Egerton RF. Radiation damage to organic and inorganic specimens in the TEM. Micron 2019;119:72–87. https://doi.org/10.1016/j.micron.2019.01.005.
[18] Jiang N. Damage mechanisms in electron microscopy of insulating materials. J Phys D: Appl Phys 2013;46:305502. https://doi.org/10.1088/0022-3727/46/30/305502.
[19] Arat KT, Klimpel T, Zonnevylle AC, Ketelaars WSMM, Heerkens, CThH, Hagen CW. Charge-induced pattern displacement in E-beam lithography. Journal of Vacuum Science & Technology B,

Nanotechnology and Microelectronics: Materials, Processing, Measurement, and Phenomena 2019;37:051603. https://doi.org/10.1116/1.5120631.
[20] Velazco A, Glen T, Klumpe S, Pennington A, Zhang J, Smith JL, et al. Reduction of SEM charging artefacts in native cryogenic biological samples 2024. https://doi.org/10.1101/2024.08.23.609373.
[21] Jiang N. Electron beam damage in oxides: a review. Rep Prog Phys 2015;79:016501. https://doi.org/10.1088/0034-4885/79/1/016501.
[22] Egerton RF. Two- and three-dimensional electron imaging of beam-sensitive specimens. Micron 2025;194:103819. https://doi.org/10.1016/j.micron.2025.103819.
[23] Vila M, Prieto C, Ramírez R. Electrical behavior of silicon nitride sputtered thin films. Thin Solid Films 2004;459:195–9. https://doi.org/10.1016/j.tsf.2003.12.082.
[24] Dow HS, Kim WS, Lee JW. Thermal and electrical properties of silicon nitride substrates. AIP Advances 2017;7:095022. https://doi.org/10.1063/1.4996314.
[25] Awan SA, Gould RD, Gravano S. Electrical conduction processes in silicon nitride thin films prepared by r.f. magnetron sputtering using nitrogen gas. Thin Solid Films 1999;355–356:456–60. https://doi.org/10.1016/S0040-6090(99)00550-7.
[26] Balland B, Glachant A. Chapter 1 Silica, silicon nitride and oxynitride thin films. Instabilities in Silicon Devices, vol. 3, Elsevier; 1999, p. 3–144. https://doi.org/10.1016/S1874-5903(99)80007-X.
[27] Bartzsch H, Glöß D, Böcher B, Frach P, Goedicke K. Properties of SiO2 and Al2O3 films for electrical insulation applications deposited by reactive pulse magnetron sputtering. Surface and Coatings Technology 2003;174–175:774–8. https://doi.org/10.1016/S0257-8972(03)00384-0.
[28] Reed ML, Fedder GK. Photolithographic Microfabrication. Handbook of Sensors and Actuators, vol. 6, Elsevier; 1998, p. 13–61. https://doi.org/10.1016/S1386-2766(98)80003-0.
[29] Ding ZJ, Li C, Da B, Liu J. Charging effect induced by electron beam irradiation: a review. Science and Technology of Advanced Materials 2021;22:932–71. https://doi.org/10.1080/14686996.2021.1976597.
[30] Andeen C, Fontanella J, Schuele D. Low-Frequency Dielectric Constant of LiF, NaF, NaCl, NaBr, KCl, and KBr by the Method of Substitution. Phys Rev B 1970;2:5068–73. https://doi.org/10.1103/PhysRevB.2.5068.
[31] Roessler DM, Walker WC. Electronic spectrum of crystalline lithium fluoride. Journal of Physics and Chemistry of Solids 1967;28:1507–15. https://doi.org/10.1016/0022-3697(67)90280-6.
[32] Jiang N. Electron beam damage in oxides: a review. Rep Prog Phys 2016;79:016501. https://doi.org/10.1088/0034-4885/79/1/016501.
[33] Colby R, Williams REA, Carpenter DL, Bagués N, Ford BR, McComb DW. Identifying and imaging polymer functionality at high spatial resolution with core-loss EELS. Ultramicroscopy 2023;246:113688. https://doi.org/10.1016/j.ultramic.2023.113688.
[34] Suzuki N, Cervera RB, Ohnishi T, Takada K. Silicon nitride thin film electrode for lithium-ion batteries. Journal of Power Sources 2013;231:186–9. https://doi.org/10.1016/j.jpowsour.2012.12.097.
[35] Huang W, Wang H, Boyle DT, Li Y, Cui Y. Resolving Nanoscopic and Mesoscopic Heterogeneity of Fluorinated Species in Battery Solid-Electrolyte Interphases by Cryogenic Electron Microscopy. ACS Energy Lett 2020;5:1128–35. https://doi.org/10.1021/acsenergylett.0c00194.
[36] Gołek F. Electron beam induced alteration of LiF thin films monitored by low energy electron transmission. Surface Science 2000;448:L188–92. https://doi.org/10.1016/S0039-6028(99)01223-6.
[37] Egerton RF, Li P, Malac M. Radiation damage in the TEM and SEM. Micron 2004;35:399–409. https://doi.org/10.1016/j.micron.2004.02.003.
[38] Egerton RF, McLeod R, Wang F, Malac M. Basic questions related to electron-induced sputtering in the TEM. Ultramicroscopy 2010;110:991–7. https://doi.org/10.1016/j.ultramic.2009.11.003.
[39] Hobbs LW. Electron-beam sensitivity in inorganic specimens. Ultramicroscopy 1987;23:339–44. https://doi.org/10.1016/0304-3991(87)90244-0.

[40] Ugurlu O, Haus J, Gunawan AA, Thomas MG, Maheshwari S, Tsapatsis M, et al. Radiolysis to knock-on damage transition in zeolites under electron beam irradiation. Phys Rev B 2011;83:113408. https://doi.org/10.1103/PhysRevB.83.113408.
[41] Xu X, Xia L, Zheng C, Liu Y, Yu D, Li J, et al. Unravelling nonclassical beam damage mechanisms in metal-organic frameworks by low-dose electron microscopy. Nat Commun 2025;16:261. https://doi.org/10.1038/s41467-024-55632-w.
[42] Susi T, Meyer JC, Kotakoski J. Quantifying transmission electron microscopy irradiation effects using two-dimensional materials. Nat Rev Phys 2019;1:397–405. https://doi.org/10.1038/s42254-019-0058-y.
[43] Jaberi A, Brodusch N, Song J, Gauvin R. Prediction of primary knock-on damage during electron microscopy characterization of lithium-containing materials. Ultramicroscopy 2024;256:113884. https://doi.org/10.1016/j.ultramic.2023.113884.
[44] Wang F, Graetz J, Moreno MS, Ma C, Wu L, Volkov V, et al. Chemical Distribution and Bonding of Lithium in Intercalated Graphite: Identification with Optimized Electron Energy Loss Spectroscopy. ACS Nano 2011;5:1190–7. https://doi.org/10.1021/nn1028168.
[45] Howitt DG, Chen SJ, Gierhart BC, Smith RL, Collins SD. The electron beam hole drilling of silicon nitride thin films. Journal of Applied Physics 2008;103:024310. https://doi.org/10.1063/1.2828157.
[46] Sickafus KE, Kotomin EA, Uberuaga BP, editors. Radiation Effects in Solids. vol. 235. Dordrecht: Springer Netherlands; 2007. https://doi.org/10.1007/978-1-4020-5295-8.
[47] Lidiard AB. The Radiolysis of Alkali Halides — the Nucleation and Growth of Aggregates. Zeitschrift Für Physikalische Chemie 1998;206:219–48. https://doi.org/10.1524/zpch.1998.206.Part_1_2.219.
[48] Song KS, Williams RT. Self-Trapped Excitons. vol. 105. Berlin, Heidelberg: Springer; 1996. https://doi.org/10.1007/978-3-642-85236-7.
[49] Liu B, Dong ZL, Hua Y, Fu C, Li X, Tan PK, et al. Electron-beam radiation induced degradation of silicon nitride and its impact to semiconductor failure analysis by TEM. AIP Advances 2018;8:115327. https://doi.org/10.1063/1.5051813.
[50] Schwartz K. Electronic excitations and defect creation in LiF crystals. Nuclear Instruments and Methods in Physics Research Section B: Beam Interactions with Materials and Atoms 1996;107:128–32. https://doi.org/10.1016/0168-583X(95)00846-2.
[51] Kabler MN, Williams RT. Vacancy-interstitial pair production via electron-hole recombination in halide crystals. Phys Rev B 1978;18:1948–60. https://doi.org/10.1103/PhysRevB.18.1948.
[52] Perez A, Davenas J, Dupuy CHS. Ionisation induced defects in alkali halide single crystals. Nuclear Instruments and Methods 1976;132:219–27. https://doi.org/10.1016/0029-554X(76)90738-2.
[53] Nahum J, Wiegand DA. Optical Properties of Some F-Aggregate Centers in LiF. Phys Rev 1967;154:817–30. https://doi.org/10.1103/PhysRev.154.817.
[54] Singh G, Gallon T. The electron energy loss spectrum of LiF in the band gap region. Solid State Communications 1984;51:281–4. https://doi.org/10.1016/0038-1098(84)90687-2.
[55] Abu-Hassan LH, Townsend PD, Wood RA. In situ optical absorption during ion-beam irradiations of LiF. Nuclear Instruments and Methods in Physics Research Section B: Beam Interactions with Materials and Atoms 1988;32:225–30. https://doi.org/10.1016/0168-583X(88)90214-5.
[56] Tadami Y, Saiki K, Koma A. Real-time observation of the surface alteration in LiF during electron irradiation. Solid State Communications 1989;70:261–4. https://doi.org/10.1016/0038-1098(89)90323-2.
[57] Okuda A. On the R Centers in Lithium Fluoride. J Phys Soc Jpn 1961;16:1746–62. https://doi.org/10.1143/JPSJ.16.1746.
[58] Kaufman JVR, Clark CD. Identification of Color Centers in Lithium Fluoride. J Chem Phys 1963;38:1388–99. https://doi.org/10.1063/1.1733863.
[59] Kunz C. Messung charakteristischer Energieverluste von Elektronen an leichtoxydierbaren Metallen im Ultrahochvakuum. Z Physik 1966;196:311–31. https://doi.org/10.1007/BF01325652.

[60] Cox PA, Williams AA. Surface excitons on ionic crystals. Surface Science Letters 1986;175:L782–6. https://doi.org/10.1016/0167-2584(86)90317-8.
[61] Creuzburg M. Energieverlustspektren der Alkalihalogenide und der Metalle Cu, Ag und Au und Vergleich mit optischen Messungen. Z Physik 1966;196:433–63. https://doi.org/10.1007/BF01380035.
[62] Creuzburg M, Raether H. On the behavior of nuclear energy losses of electrons in alkali halides. Solid State Communications 1964;2:175–7. https://doi.org/10.1016/0038-1098(64)90108-5.
[63] Boniface M, Quazuguel L, Danet J, Guyomard D, Moreau P, Bayle-Guillemaud P. Nanoscale Chemical Evolution of Silicon Negative Electrodes Characterized by Low-Loss STEM-EELS. Nano Lett 2016;16:7381–8. https://doi.org/10.1021/acs.nanolett.6b02883.
[64] Koh H, Das S, Zhang Y, Detsi E, Stach EA. Electron Beam-Induced Artifacts in SEI Characterization: Evidence from Controlled-Dose Diffraction Studies. ACS Energy Lett 2025:534–40. https://doi.org/10.1021/acsenergylett.4c03337.
[65] Lin F, Markus IM, Doeff MM, Xin HL. Chemical and Structural Stability of Lithium-Ion Battery Electrode Materials under Electron Beam. Sci Rep 2014;4:5694. https://doi.org/10.1038/srep05694.
[66] Bai S, Liu Z, Cheng D, Lu B, Zaluzec NJ, Raghavendran G, et al. Guidelines for correlative imaging and analysis of reactive alkali metal battery materials. Joule 2026:102311. https://doi.org/10.1016/j.joule.2025.102311.
[67] Ilett M, S'ari M, Freeman H, Aslam Z, Koniuch N, Afzali M, et al. Analysis of complex, beam-sensitive materials by transmission electron microscopy and associated techniques. Phil Trans R Soc A 2020;378:20190601. https://doi.org/10.1098/rsta.2019.0601.
[68] Li X, Dyck O, Kalinin SV, Jesse S. Compressed Sensing of Scanning Transmission Electron Microscopy (STEM) With Nonrectangular Scans. Microanal 2018;24:623–33. https://doi.org/10.1017/S143192761801543X.
[69] Velazco A, Nord M, Béché A, Verbeeck J. Evaluation of different rectangular scan strategies for STEM imaging. Ultramicroscopy 2020;215:113021. https://doi.org/10.1016/j.ultramic.2020.113021.
[70] Zobelli A, Woo SY, Tararan A, Tizei LHG, Brun N, Li X, et al. Spatial and spectral dynamics in STEM hyperspectral imaging using random scan patterns. Ultramicroscopy 2020;212:112912. https://doi.org/10.1016/j.ultramic.2019.112912.
[71] Hollenbach JD, Koppell S, Smalley D, Francis C, Levin BDA, Macy J, et al. Beam teleportation for precision dose control in scanning transmission electron microscopy. Ultramicroscopy 2026:114371. https://doi.org/10.1016/j.ultramic.2026.114371.
[72] Bammes B, Moore K, Levin BDA. Physics-Based Scan Distortion Correction in Hardware. Microscopy and Microanalysis 2024;30:ozae044.1088. https://doi.org/10.1093/mam/ozae044.1088.
[73] Peters JJP, Moldovan G, Jones L. Towards Cinematic STEM and Beyond: Fast Frame Rates Using Overdriven Scan Shaping. Microscopy and Microanalysis 2025;31:ozaf048.915. https://doi.org/10.1093/mam/ozaf048.915.
[74] Egerton RF. Scattering delocalization and radiation damage in STEM-EELS. Ultramicroscopy 2017;180:115–24. https://doi.org/10.1016/j.ultramic.2017.02.007.
[75] Sang X, Lupini AR, Unocic RR, Chi M, Borisevich AY, Kalinin SV, et al. Dynamic scan control in STEM: spiral scans. Adv Struct Chem Imag 2016;2:6. https://doi.org/10.1186/s40679-016-0020-3.
[76] Kovarik L, Stevens A, Liyu A, Browning ND. Implementing an accurate and rapid sparse sampling approach for low-dose atomic resolution STEM imaging. Applied Physics Letters 2016;109:164102. https://doi.org/10.1063/1.4965720.
[77] Jannis D, Velazco A, Béché A, Verbeeck J. Reducing electron beam damage through alternative STEM scanning strategies, Part II: Attempt towards an empirical model describing the damage process. Ultramicroscopy 2022;240:113568. https://doi.org/10.1016/j.ultramic.2022.113568.

[78] Velazco A, Béché A, Jannis D, Verbeeck J. Reducing electron beam damage through alternative STEM scanning strategies, Part I: Experimental findings. Ultramicroscopy 2022;232:113398. https://doi.org/10.1016/j.ultramic.2021.113398.
[79] Peters JJP, Mullarkey T, Gott JA, Nelson E, Jones L. Interlacing in Atomic Resolution Scanning Transmission Electron Microscopy. Microscopy and Microanalysis 2023;29:1373–9. https://doi.org/10.1093/micmic/ozad056.
[80] Thong JTL, Lee KW, Wong WK. Reduction of charging effects using vector scanning in the scanning electron microscope. Scanning 2001;23:395–402. https://doi.org/10.1002/sca.4950230606.
[81] Egerton RF. Two- and three-dimensional electron imaging of beam-sensitive specimens. Micron 2025;194:103819. https://doi.org/10.1016/j.micron.2025.103819.
[82] Moshtaghpour A, Velazco-Torrejon A, Nicholls D, Robinson AW, Kirkland AI, Browning ND. Diffusion distribution model for damage mitigation in scanning transmission electron microscopy. Journal of Microscopy 2025;297:57–77. https://doi.org/10.1111/jmi.13351.
[83] Nicholls D, Lee J, Amari H, Stevens AJ, Mehdi BL, Browning ND. Minimising damage in high resolution scanning transmission electron microscope images of nanoscale structures and processes. Nanoscale 2020;12:21248–54. https://doi.org/10.1039/d0nr04589f.
[84] Ruíz TF, García-Fernández P, Aramburu JA, Moreno M, Lysgaard S, García-Lastra JM. Dynamics of the electron-hole separation of the fundamental exciton in LiF. Phys Rev B 2025;112:054308. https://doi.org/10.1103/mqqw-qz5d.
[85] Nakonechnyi S, Kärner T, Lushchik A, Lushchik C, Babin V, Feldbach E, et al. Low-temperature excitonic, electron–hole and interstitial-vacancy processes in LiF single crystals. J Phys: Condens Matter 2005;18:379. https://doi.org/10.1088/0953-8984/18/2/003.
[86] Egerton RF. Measurement of radiation damage by electron energy-loss spectroscopy. Journal of Microscopy 1980;118:389–99. https://doi.org/10.1111/j.1365-2818.1980.tb00288.x.
[87] White ER, Mecklenburg M, Shevitski B, Singer SB, Regan BC. Charged Nanoparticle Dynamics in Water Induced by Scanning Transmission Electron Microscopy. Langmuir 2012;28:3695–8. https://doi.org/10.1021/la2048486.
[88] Egerton R. Radiation Damage and Nanofabrication in TEM and STEM. Micros Today 2021;29:56–9. https://doi.org/10.1017/S1551929521000663.
[89] Han B, Li X, Bai S, Zou Y, Lu B, Zhang M, et al. Conformal three-dimensional interphase of Li metal anode revealed by low-dose cryoelectron microscopy. Matter 2021;4:3741–52. https://doi.org/10.1016/j.matt.2021.09.019.
[90] Ortiz D, Steinmetz V, Durand D, Legand S, Dauvois V, Maître P, et al. Radiolysis as a solution for accelerated ageing studies of electrolytes in Lithium-ion batteries. Nat Commun 2015;6:6950. https://doi.org/10.1038/ncomms7950.